2016

Second Harmonic Generation Imaging of a Magnetic Topological Insulator

Carina Belvin
cbelvin@wellesley.edu

Second Harmonic Generation Imaging of a Magnetic Topological Insulator

Carina Belvin

Submitted in Partial Fulfillment of the
Prerequisite for Honors in Physics

Advisors:
Nuh Gedik, MIT
Robbie Berg, Wellesley College

April 2016

Wellesley College

Abstract

A topological insulator (TI) is a type of quantum material that is insulating in the bulk but metallic on the surface. Due to the unique spin properties of the surface electrons, TIs have attracted much interest for their potential applications in spin-based electronics and quantum computers. Even more exotic effects occur when TIs are brought in contact with magnetic materials. This thesis represents a study of two-layer thin films consisting of the TI Bi_2Se_3 and the magnetic insulator EuS using a nonlinear optical technique called second harmonic generation (SHG) imaging. SHG imaging can probe the crystal and magnetic structure at the surfaces and interfaces of inversion symmetric materials. At the interface between the EuS and Bi_2Se_3 layers, magnetic domains are expected to form. The domain boundaries are predicted to host chiral edge states, which are dissipationless currents that flow in one direction around a domain. Using SHG imaging, our goal was to visualize the magnetic domains in this magnetic topological insulator system. Even though we have yet to observe any evidence of magnetic domains in this material, we also performed SHG imaging on monolayer MoS_2 and were able to visualize distinct crystal grains. Our SHG imaging setup that was improved upon during this thesis has the potential to reveal information about other interesting quantum materials.

Acknowledgements

First, I would like to thank my advisor at MIT, Professor Nuh Gedik, for the opportunity to conduct my senior thesis research in his lab and for his support throughout this past year as an advisor and mentor. Thank you as well to graduate student Changmin Lee for all of his help with this thesis project, from experimental guidance to thesis revisions. I am grateful to all of the members of the Gedik lab for their advice, support, and kindness. I am excited to join the Gedik group as a graduate student next year!

I would like to thank my Wellesley thesis advisor, Professor Robbie Berg, for his guidance throughout this project. I am very grateful for all of the support that he has given me throughout my time at Wellesley, as a research advisor, professor, and mentor. I also thank the members of my thesis committee, Professor Glenn Stark, Professor Jerome Fung, and Professor Megan Kerr.

Additionally, I would like to acknowledge Ferhat Katmis, in Jagadeesh Moodera's group, and Yi-Hsien Lee, a former member of Jing Kong's group, both at MIT, for providing the samples used in these experiments.

Funding for this thesis was generously provided by the Jerome A. Schiff Fellowship. This work was part of the Center for Integrated Quantum Materials (CIQM).

Contents

List of Figures

Chapter 1

Introduction

Quantum materials exhibit fascinating physical properties that also have the potential to be exploited for new applications. A topological insulator (TI) is a type of quantum material that is insulating in the bulk but metallic on the surface, where the electrons possess unique properties. Even more exotic effects occur when a TI is placed in contact with a magnetic material. The goal of this thesis is to investigate heterostructures of Bi_2Se_3, a topological insulator, and EuS, a ferromagnetic insulator.

Light can be a useful tool for probing the electronic properties of quantum materials. The technique used in this thesis is a type of nonlinear optical microscopy called second harmonic generation (SHG) imaging. SHG imaging can probe the lattice and magnetic structure of certain materials and can reveal information that cannot be obtained by conventional linear microscopy.

The first portion of my thesis involved making improvements to the existing SHG imaging setup in the Gedik lab. Then, we tested the functionality of our setup using the two-dimensional material MoS_2. The main portion of my thesis was searching for evidence of magnetic domains in EuS/Bi_2Se_3 heterostructures using SHG imaging.

1.1 Quantum Materials

Quantum materials is a term used to describe a broad class of materials that demonstrate novel properties due to quantum mechanical effects. Classically, matter is characterized by its phase, such as solid, liquid, or gas. When quantum mechanics is introduced, however, other phases come into play. One of the goals of condensed matter physics is to understand these quantum phases of matter, which include superconductors, ferromagnets, Bose-Einstein condensates, charge density waves, and others [1].

Crystalline solids are composed of a periodic array of atoms. The complex interactions of the large numbers of ions and electrons in a solid lead to different phases. Phases of matter are generally characterized by the symmetries that they possess, which can include rotational, mirror, inversion, and time-reversal symmetry. Ferromagnets, for example, break time-reversal symmetry: when the direction of time is reversed, the system does not appear the same.

In the 1980s, a new, topological type of order was discovered through what is known as the quantum Hall effect. The quantum Hall effect occurs when electrons are confined to two-dimensions and subject to a strong perpendicular magnetic field, and it results in current flow along the edge of the two-dimensional material [2]. Special properties of topological order include dissipationless flow of current and emergent particles with fractional charge [2]. It has also been discovered that topological order can occur in three-dimensional materials. Spin-orbit coupling plays the role of the magnetic field in these materials. These materials are called topological insulators because they are insulating in the bulk but possess novel metallic states on the surface due to topological order [2]. The surface currents are chiral, meaning that they flow in only one direction. Electrons with opposite spins flow in opposite directions, and hence the surface states of topological insulators are said to be topologically protected.

Another important class of quantum materials is two-dimensional (2D) materials. These include graphene and other materials that are a single atom thick. The electrons in

graphene have a linear energy-momentum dispersion and are described by the Dirac equation, the relativistic analog to the Schrödinger equation. Another class of 2D materials are the transistion metal dichalcogenides (TMDs), compounds consiting of a transition metal and a calcogen, a member of group 16 in the periodic table (the oxygen family). Monolayers of 2D materials can be assembled into heterostructures that are held together by van der Waals forces.

Quantum materials such as topological insulators and 2D materials are appealing not only for the wealth of new physics that they provide but also for their potential use in applications ranging from spin-based electronics ("spintronics"), a type of electronics that utilizes electron spin rather than electron charge, to quantum computing. To this end, the Center for Integrated Quantum Materials (CIQM), a collaboration between Harvard, MIT, and Howard University as well as several colleges including Wellesley College, has been investigating the properties of quantum materials and how their functionalities can be integrated to create quantum computers and other novel types of electronic devices. For example, 2D materials can be used for high-speed, low-power transistors and flexible electronics. Topological insulators can function as protected data channels in quantum computers (due to their topologically protected surface states) and can be used in spintronic devices. A third category of quantum materials that is being pursued by CIQM is nitrogen-vacancy (NV) centers in diamond. The spin state of an NV center can serve as a single quantum bit for quantum computers owing to its long coherence time (information can be stored for more than 1 millisecond at room temperature) and that it can be manipulated and read out optically with a laser. Additionally, an NV center can act as a single photon source and therefore can be used in photonics.

1.2 Topological Insulators

A topological insulator (TI) is a type of quantum material that is insulating in the bulk yet supports metallic states on the surface. There are two classes of TIs: two-dimensional

(2D) and three-dimensional (3D) TIs. A 3D TI is a 3D bulk insulator that contains 2D metallic surface states. In 2D TIs, a 2D insulator is surrounded by 1D conducting edges. Similar to a quantum Hall system, the edge states of a 2D TI are helical; the spin up electrons only move in a certain direction and the spin down electrons only move in the opposite direction, as illustrated in Figure 1.1(a) [3]. Rather than the strong perpendicular magnetic field required for the quantum Hall effect, the chiral edge channels in TIs are a result of strong spin-orbit coupling in the material. Spin-orbit coupling is the coupling between an electron's spin and its orbital angular momentum. Atoms with large atomic numbers, such as bismuth (Bi), have strong spin-orbit coupling. In contrast to a quantum Hall state, TIs possess time reversal symmetry, namely, when time is reversed, the system remains the same. We can see that this is true from Figure 1.1(a), since reversing time reverses both the spin of electrons and their direction of motion. Therefore, we say that the chiral edge states are topologically protected by time-reversal symmetry. Another consequence of spin-orbit coupling in TIs is that the surface electrons are insensitive to scattering by nonmagnetic impurities. Furthermore, the chiral edge states are dissipationless as in a quantum Hall system.

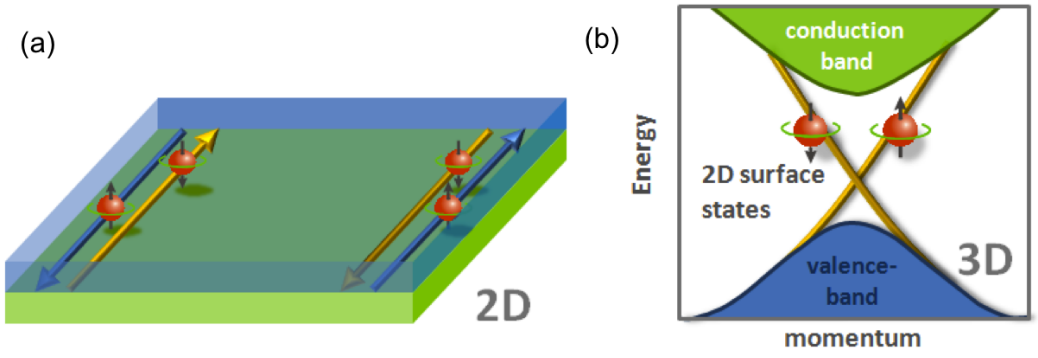

FIGURE 1.1: (a) Diagram of a 2D TI showing the counter-propagating edge currents. (b) Band structure of a 3D TI. (Figure taken from [3].)

The band structure of a TI is shown in Figure 1.1(b) [3]. Since the bulk of the TI is an insulator, there is a gap between the bulk valence band and the bulk conduction band. The metallic surface states, in contrast, are gapless and have a linear energy-momentum dispersion. The cartoon of electron spins drawn in the diagram indicates that electrons with opposite spins have opposite directions of their momentum. The spin

direction in fact is locked perpendicular to the momentum direction, which is due to spin-orbit coupling. A consequence of this is that surface electrons do not backscatter off of non-magnetic impurities. The presence of time-reversal symmetry in TIs protects these surface states.

Even more unique properties of TIs occur when perturbations induce an energy gap in the surface states. When a TI is placed in proximity to a superconductor, it is predicted to host Majorana fermion excitations [4]. A Majorana fermion is a particle that is its own antiparticle. When a TI is instead subject to magnetic perturbations, time-reversal symmetry is broken. This can be accomplished by the application of an external magnetic field, by proximity to a magnetic material such as a ferromagnet, or by doping with magnetic impurities. The magnetic perturbation induces magnetic domains on the surface of the TI and the boundaries between magnetic domains are predicted to host one-dimensional dissipationless chiral edge states [4]. A drawing of two magnetic domains separated by a chiral edge state is shown in Figure 1.2 [4]. The strength of an applied magnetic field ordinarily needs to be a few tens of Tesla in order to observe these effects. Various other phenomena that have been predicted to occur in magnetic topological insulator systems include massive Dirac fermions [5], the topological magnetoelectric effect [4] [6], the quantum anomalous Hall effect [4], and an image magnetic monopole [7].

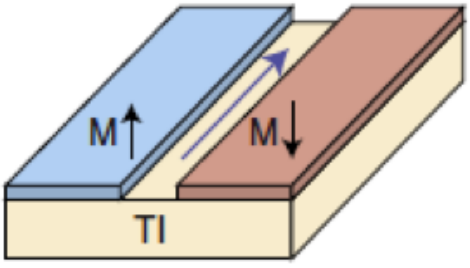

FIGURE 1.2: Drawing of a TI with two magnetic domains on its surface separated by a chiral edge current (blue arrow). (Figure taken from [4].)

1.3 Nonlinear Optics

Nonlinear optics is the study of the nonlinear interaction of light with a material. The response of a material to an applied optical field is nonlinear in terms of its dependence on the strength of the optical field. In linear optics, the induced polarization in a material, the electric dipole moment per unit volume, is given by

$$P(t) = \epsilon_0 \chi^{(1)} E(t), \tag{1.1}$$

where $E(t)$ is the electric field of the incident light as a function of time, $\chi^{(1)}$ is the linear susceptibility, and ϵ_0 is the permittivity of free space [8]. In other words, the induced polarization depends linearly on the incident electric field strength. A quadratic or higher order dependence on the electric field indicates a nonlinear response, and this is the realm of nonlinear optics.

The induced polarization in a nonlinear medium is the generalization of Equation 1.1 as a power series expansion in the electric field $E(t)$:

$$P(t) = \epsilon_0(\chi^{(1)} E(t) + \chi^{(2)} E^2(t) + \chi^{(3)} E^3(t) + \dots), \tag{1.2}$$

where $\chi^{(2)}$ is the second-order nonlinear susceptibility and $\chi^{(3)}$ is the third-order nonlinear susceptibility [8]. These two equations are in scalar form, so the quantities $\chi^{(1)}$, $\chi^{(2)}$, and $\chi^{(3)}$ are scalars. In vector form, $\chi^{(1)}$ is a second-rank tensor (also known as a matrix), $\chi^{(2)}$ is a third-rank tensor, and $\chi^{(3)}$ is a fourth-rank tensor. Each nonlinear susceptibility tensor contains information about the lattice and electronic symmetries of a crystal, with each higher-order tensor providing more detail due to the larger number of tensor elements.

Polarization is an important quantity in nonlinear optics because a time-varying polarization can lead to the generation of electromagnetic radiation. The wave equation in a nonlinear medium with index of refraction n and induced polarization $P(t)$ is given

by

$$\nabla^2 E - \frac{n^2}{c^2}\frac{\partial^2 E}{\partial t^2} = \frac{1}{\epsilon_0 c^2}\frac{\partial^2 P}{\partial t^2}. \tag{1.3}$$

From this equation, we can see that when $P(t)$ oscillates in time, electromagnetic radiation is produced. Different terms in the equation for $P(t)$ (Equation 1.2) contribute different frequencies of radiation. In fact, when light of frequency ω is incident on a material, the frequencies of radiation that are produced are higher harmonics of the incident frequency, $n\omega$, where n is an integer. This process is known as nonlinear harmonic generation (NHG) [9]. Due to the very low NHG efficiency of most materials, high-intensity laser light is required in order to produce higher harmonic radiation.

1.4 Second Harmonic Generation (SHG)

The second term in Equation 1.2, $P^{(2)}(t) = \epsilon_0 \chi^{(2)} E^2(t)$, is known as the second-order nonlinear polarization [8]. Consider an arbitrary applied electric field from a laser beam, $E(t) = Ee^{i\omega t} + c.c.$ Then the second-order nonlinear polarization is given by

$$\begin{aligned} P^{(2)}(t) &= \epsilon_0 \chi^{(2)} E^2(t) \\ &= 2\epsilon_0 \chi^{(2)} E E^* + (\epsilon_0 \chi^{(2)} E^2 e^{-i2\omega t} + c.c.). \end{aligned} \tag{1.4}$$

The first term is a constant (independent of frequency), while the second term has frequency 2ω. From Equation 1.3, we see that the first term does not produce any radiation, while the second terms leads to radiation of frequency 2ω, the second harmonic of the incident light. Hence, this process is called second harmonic generation (SHG). We can think of SHG as the conversion of an incident frequency of light to double that frequency, i.e. frequency doubling. The first experimental evidence for SHG was demonstrated by Franken et al. in 1961 using a ruby maser and crystalline quartz [10]. One application of SHG commonly used today in the laser industry is in green 532 nm diode-pumped solid state lasers (DPSSLs). Nd:YAG lasers produce 1064 nm light, and the frequency is doubled (the wavelength is halved) through SHG to output 532 nm light [8].

We can also view the SHG process from a quantum mechanics perspective as the interaction of photons rather than waves. Two photons of frequency ω come together and a photon of frequency 2ω is created in their place. An energy diagram of this process is shown in Figure 1.3 [8]. The solid line at the bottom is the atomic ground state and the dashed lines above it are virtual levels, which are at energies that are the combination of an atomic energy level and the energy of the photon.

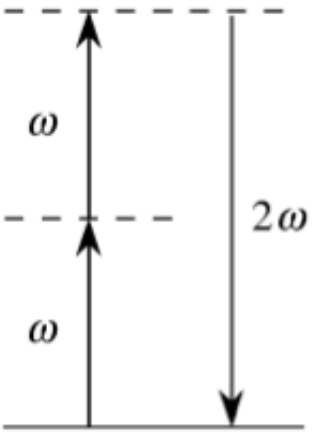

FIGURE 1.3: Energy diagram of the SHG process. A photon of frequency 2ω results from the combination of two photons, each of frequency ω. (Figure adapted from [8].)

NHG processes depend on the symmetries of a crystal. SHG in particular is sensitive to inversion symmetry breaking. A crystal possesses inversion symmetry, or is centrosymmetric, if it contains an inversion center. An inversion center is a point such that if you consider any other atom in the crystal and draw a vector from the inversion center to that atom, then there is an identical atom lying at the tip of the negative of that vector. If inversion symmetry is absent in a crystal, then the dominant contribution to the SHG signal is electric dipolar radiation. However, in noncentrosymmetric crystals, electric dipolar radiation is not allowed, so the dominant contribution to the SHG signal is electric quadrupolar radiation, which is much smaller in magnitude than electric dipolar radiation. Therefore, SHG is useful for distinguishing parts of a sample that are not inversion symmetric from parts that are inversion symmetric.

1.5 Using SHG to Study Quantum Materials

SHG can reveal not only lattice symmetries but also magnetic symmetries. In particular, SHG can be used to probe the surfaces and interfaces of layers of materials that are centrosymmetric, since inversion symmetry is by definition broken at any surface or interface. Below are a couple of quantum material systems that have been studied using SHG.

1.5.1 Bi_2Se_3

Bismuth selenide (Bi_2Se_3) is a 3D TI. The crystal structure of Bi_2Se_3 consists of quintuple layers (QL), where a unit cell (the smallest portion of the lattice that can be repeated and translated to produce the entire lattice) is 3 QL (Figure 1.4) [11]. Bi_2Se_3 has threefold rotational symmetry about the z-axis, which can be seen in Figure 1.4(b). A single quintuple layer consists of the five layers Se1-Bi1-Se2-Bi1′-Se1′. The selenium atoms in the Se2 layer, shown in yellow in Figure 1.4(c), are inversion centers, so the bulk of Bi_2Se_3 is centrosymmetric. However, inversion symmetry is necessarily broken at the surface, which allows the surface states of the TI to be probed using SHG.

Hsieh et al. demonstrated that SHG can probe both the lattice symmetry at the surface and the surface charge of Bi_2Se_3 [12]. Optical techniques are advantageous because they are contact-free. Previous transport measurements of Bi_2Se_3 and related materials had been unable to separate the bulk and surface signals, and previous optical measurements had been restricted to the linear regime, which is dominated by the signal from the bulk. Hsieh et al. used the nonlinear optical technique of SHG to selectively probe the signal from the surface of Bi_2Se_3.

Figure 1.5(a) shows the reflection geometry of their SHG measurements. The measurements they performed are known as rotational anisotropy (RA) measurements. In this technique, the scattering plane of light (in yellow), which is the plane formed by

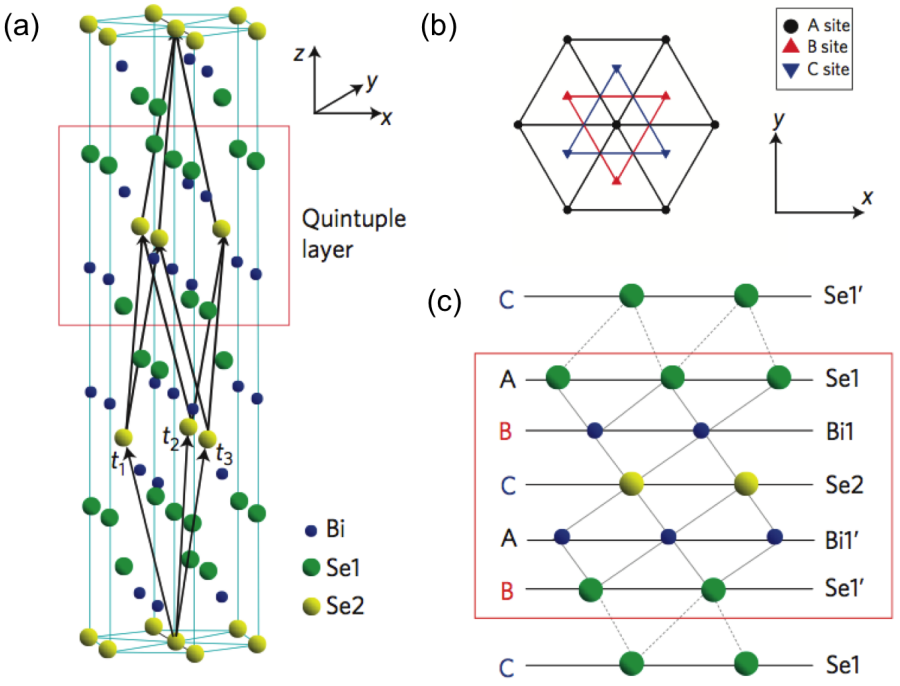

FIGURE 1.4: Crystal structure of Bi_2Se_3. (a) The three primitive lattice vectors are denoted by t_1, t_2, and t_3. (Primitive lattice vectors are linearly independent vectors whose linear combinations produce all of the atoms of the lattice.) A single quintuple layer is boxed in red. (b) Top view of the crystal structure. Bi_2Se_3 has threefold rotational symmetry about the z-axis. (c) Side view of the quintuple layer, which consists of the five layers Se1-Bi1-Se2-Bi1′-Se1′. From the structure we can see that the yellow selenium atoms in the Se2 layer are centers of inversion, and therefore the bulk of Bi_2Se_3 is centrosymmetric. The layers Bi1′ and Se1′ can be obtained by inverting the layers Bi1 and Se1, respectively, about the yellow Se2 atoms. (Figure taken from [11].)

the incident and reflected beams, is rotated with respect to the crystal axes. The SHG intensity is then recorded as a function of the angle ϕ. The direction of the polarization of the incoming light can be set as parallel (P) or perpendicular (S) to the scattering plane. Similarly, the P or S component of the SHG signal from the sample can be detected. An example of an SHG RA plot in the S_{in}-S_{out} geometry is shown in Figure 1.6. This polar plot has threefold rotational symmetry, which reflects the threefold rotational symmetry of the surface crystal structure of Bi_2Se_3. By analyzing the SHG data for all four geometries (P_{in}-P_{out}, S_{in}-P_{out}, P_{in}-S_{out}, and S_{in}-S_{out}), they were able to determine all of the components of the nonlinear optical susceptibility tensor, which contains all of the symmetry operations present in the crystal. Since their samples were bulk Bi_2Se_3 crystals,

which are bulk inversion symmetric, the dominant contribution to the SHG signal was from the surface, where inversion symmetry is broken. Hence, SHG RA measurements are an effective probe of the crystalline symmetry of the surface of a centrosymmetric material.

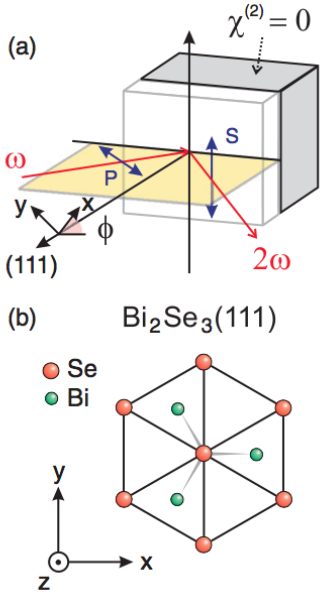

FIGURE 1.5: (a) Reflection geometry of the SHG RA setup. (b) Crystal structure of the $Bi_2Se_3(111)$ surface, which shows the threefold rotational symmetry about the z-axis. (Figure taken from [12].)

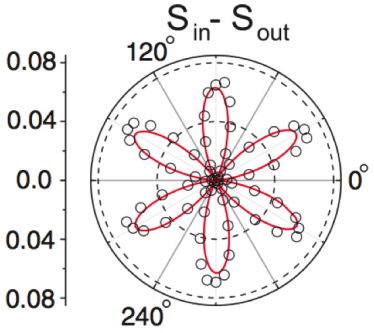

FIGURE 1.6: Polar plot from an SHG RA measurement in the S_{in}-S_{out} geometry. The threefold rotational symmetry in the plot reflects the threefold rotational lattice symmetry at the surface of Bi_2Se_3. (Figure taken from [12].)

Hsieh et al. also demonstrated that SHG is sensitive to the Fermi level (the energy of the most energetic electrons) of the surface. They tuned the surface Fermi level by depositing O_2 (an electron acceptor) onto the surface of their Bi_2Se_3 crystals and then measured the SHG signal as a function of time. Additionally, they showed that SHG

can probe time-reversal symmetry at the surface by measuring circular dichroism, which is the difference in the absorption of left and right circularly polarized light, and that this measurement does not depend on surface charging. Their results offered a promising technique for studying the surfaces of TIs, which could be extended to interfaces between TIs and other materials.

1.5.2 MoS_2

Molybdenum disulfide (MoS_2) is a TMD. Similar to graphite, which is composed of stacked layers of two-dimensional graphene, TMD crystals consist of monolayers bound together by van der Waals attractions. However, unlike graphene, the monolayers of TMDs have a band gap of 1.8 eV (in the visible region) and can therefore be used as semiconductors for nanoelectronic and optoelectronic devices [13]. The crystal structure of MoS_2 consists of two layers of sulfur atoms each in a two-dimensional hexagonal lattice with a layer of molybdenum atoms in between, as shown in Figure 1.7 [14]. When viewed from above, as in Figure 1.7(b), the crystal structure appears to be a two-dimensional honeycomb lattice consisting of two different atoms. A honeycomb lattice that has two inequivalent atoms will have two different maxima/minima in the valence/conduction bands known as valleys. These two different valleys can be utilized in applications known as "valleytronics," where the two valleys play a similar role to up and down spins in spintronic devices. MoS_2 exhibits circular dichroism, meaning the two inequivalent valleys absorb left and right circularly polarized light differently. Hence, monolayer MoS_2 has emerged as an excellent candidate for the realization of valleytronic devices [14].

The techniques for studying TMDs such as MoS_2 have typically been limited to scanning tunneling microscopy (STM) and transmission electron microscopy (TEM). However, in 2014, Yin et al. used SHG imaging to visualize the crystal grains and grain boundaries in polycrystalline monolayers of MoS_2 [13]. Since a monolayer of MoS_2 is non-centrosymmetric, it produces a strong SHG signal. Yin et al. used monolayers of MoS_2

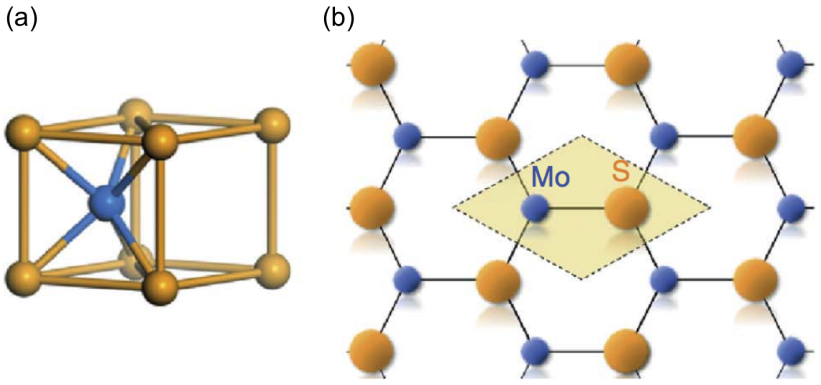

FIGURE 1.7: Crystal structure of MoS_2. (a) A portion of the two hexagonal layers of sulfur atoms with a molybdenum atom in between. (b) Top view of the crystal structure, which shows that it is a honeycomb lattice. The yellow diamond indicates the unit cell. (Figure taken from [14].)

grown by chemical vapor deposition (CVD) for their imaging experiments. A comparison of their linear and SHG images is shown in Figure 1.8. The linear image shown in Figure 1.8(a) is uniform across the entire sample (the white scale bar represents 40 μm). However, the SHG image shown in Figure 1.8(b) of the same sample area shows clear irregular-shaped patches separated by dark boundaries, indicating that the monolayer is in fact polycrystalline. The average size of the single crystal grains is between 20 μm and 40 μm. The grains appear bright due to their strong SHG, while the grain boundaries appear dark due to the destructive interference of second harmonic waves originating from adjacent grains that have different crystal orientations. Figure 1.8(c) is the same as Figure 1.8(b) except that the grains are color coded according to their crystal orientations, which are determined by rotational anisotropy measurements. Figure 1.8(d) shows the actual direction of the crystal axes of the grains in three different areas of the sample labeled in Figure 1.8(c). The crystal orientations determined by SHG matched well with those obtained by TEM measurements. SHG imaging therefore provides a direct way of identifying the orientation of single crystal grains within a polycrystalline sheet of monolayer MoS_2. The technique of SHG imaging will be discussed in more detail in Chapter 2.

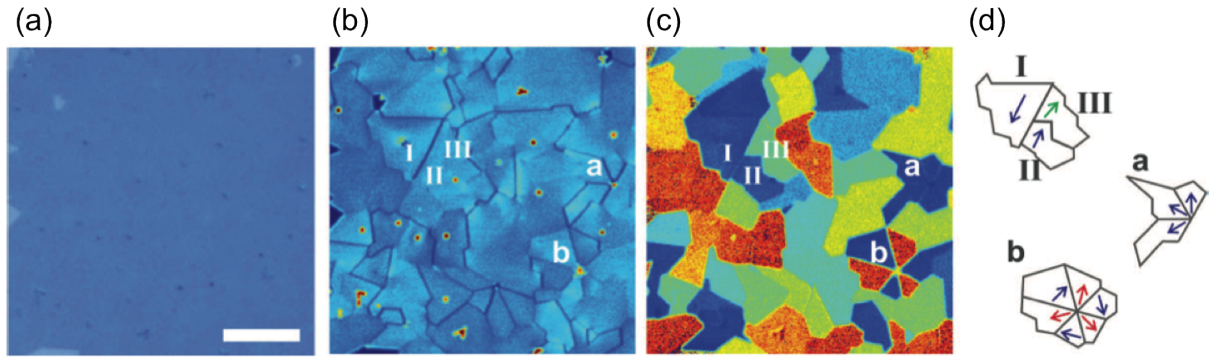

FIGURE 1.8: SHG imaging data of CVD-grown monolayer MoS_2. (a) Linear image of the sample, which is uniform. The white scale bar represents 40 μm. (b) SHG image showing single crystal grains in different crystal orientations separated by grain boundaries. (c) Same image as (b) but color coded according to the crystal orientation of the grains. (d) Select regions of the sample showing the actual crystal orientation vector of the grains. (Figure taken from [13].)

1.5.3 EuS/Bi_2Se_3 Heterostructures

EuS is an insulator that is ferromagnetic below $T_{Curie} = 17$ K. When a layer of EuS is placed in contact with Bi_2Se_3, a 3D TI, a canted magnetic moment is induced at the interface between the two layers and time-reversal symmetry is broken [6]. A "canted" moment means that the magnetic moment has both an in-plane and an out-of-plane component, as shown in Figure 1.9. The out-of-plane moments are what breaks time-reversal symmetry since the surface states are 2D. These magnetic moments form magnetic domains whose boundaries can host chiral edge states, which are one-way moving, dissipationless currents analogous to the edge currents in a quantum Hall system. The motivation for growing a layer of EuS on top of the Bi_2Se_3 surface to induce magnetism rather than through the doping of magnetic impurities, as was common in previous experimental studies, is that doping induces scattering and crystal defects, thereby reducing the mobility of the surface electrons [6]. The layer of EuS induces magnetism uniformly across the Bi_2Se_3 surface and is a much cleaner alternative to magnetic doping.

Lee et al. performed SHG RA measurements on EuS/Bi_2Se_3 heterostructures and was able to directly measure both the in-plane and out-of-plane magnetism that is induced at the interface [15]. Figure 1.10 shows the geometry of SHG RA measurements using an

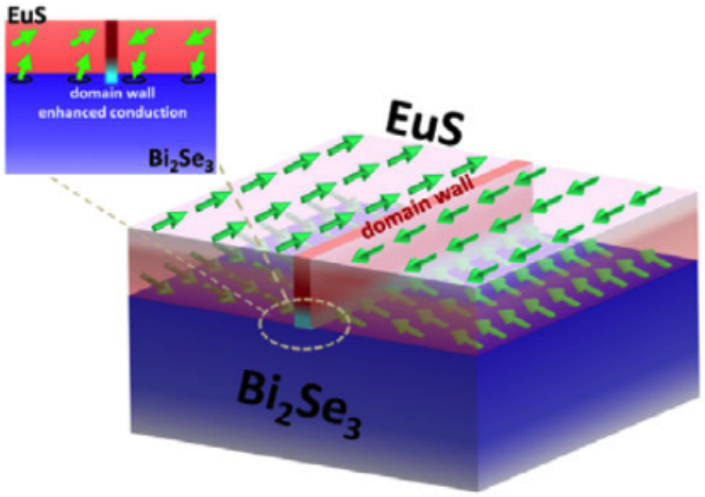

FIGURE 1.9: Diagram of a EuS/Bi_2Se_3 heterostructure. The green arrows represent the magnetic moments. The moments at the interface between the EuS and Bi_2Se_3 layers are canted (have both in-plane and out-of-plane components). (Figure taken from [6].)

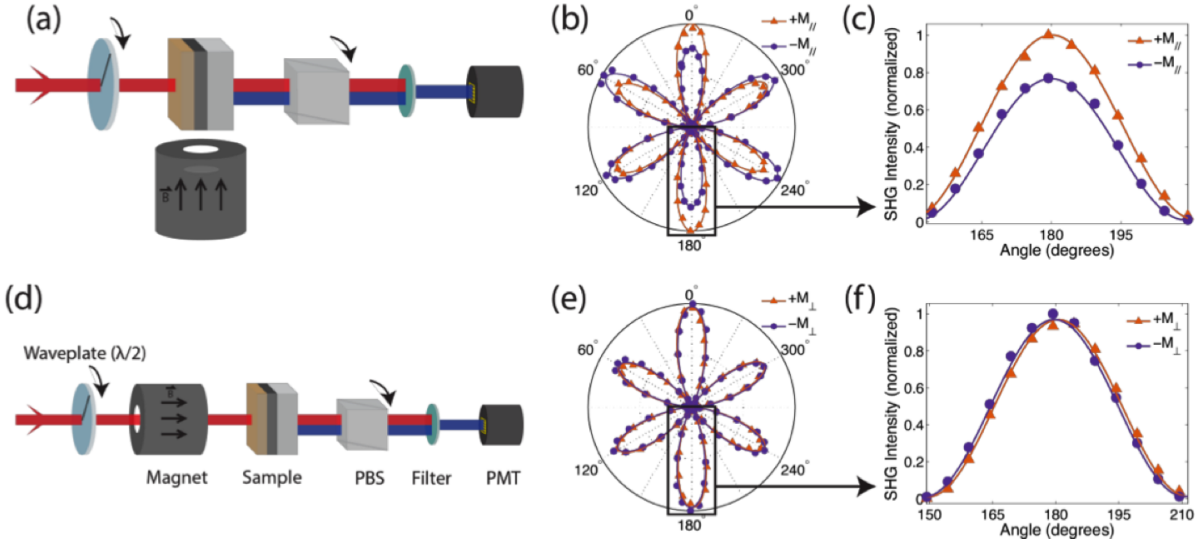

FIGURE 1.10: SHG RA data of EuS/Bi_2Se_3 heterostructures. (a) Schematic of the experimental geometry for in-plane magnetic field experiments. (b) RA plot with an in-plane magnetic field. The orange data represents an applied magnetic field of +300 Gauss and the purple data represents −300 Gauss. (c) A single petal of the RA pattern in (b) shows the difference in intensity when the magnetic field is applied in opposite directions. (d) Schematic of the geometry for out-of-plane magnetic field experiments. (e) RA plot with an out-of-plane magnetic field. The orange data represents a field of +400 Gauss and the purple data represents −400 Gauss. (f) A single petal of the RA pattern in (e) shows a slight rotation of the pattern as the direction of the magnetic field is reversed. (Figure taken from [15].)

in-plane (a) and out-of-plane (d) magnetic field. The data taken by applying an in-plane magnetic field of +300 Gauss (in orange) and −300 Gauss (in purple) is shown in (b). We can observe a twofold magnetic symmetry in addition to the threefold crystal symmetry of the Bi_2Se_3 surface (see Figure 1.6). Figure 1.10(c) illustrates the difference in SHG intensity when the direction of the magnetic field is reversed. In Figure 1.10(e) and (f), an out-of-plane magnetic field of +400 Gauss (in orange) and −400 Gauss (in purple) was applied, and the result is a slight rotation of the RA pattern [15].

The goal of my thesis is to investigate this same material system using SHG imaging to visualize the magnetic domains at the interface and possibly also the chiral edge states that reside along the domain boundaries.

Chapter 2

Experimental Technique

This thesis represents my work on improving the Gedik lab's existing SHG imaging setup, testing the setup using monolayer MoS_2 samples and comparing our data to the previous literature on SHG imaging of MoS_2 [14], and using the SHG imaging setup to investigate the magnetic domains at the interface of EuS/Bi_2Se_3 heterostructures. This chapter discusses the experimental technique of SHG imaging, our setup, and the improvements that we made to the setup during the course of this thesis.

2.1 Magnetic Second Harmonic Generation Imaging

Magnetic second harmonic generation (MSHG) imaging is a useful probe of magnetism at surfaces and interfaces. It is particularly useful for studying materials systems in which the magnetism at the surface or interface is different from that of the bulk. Kirilyuk et al. demonstrated that nonlinear optical microscopy can complement linear microscopy using magnetic garnet films [16]. In this study, a thin (~ 10 μm) layer of garnet was epitaxially grown on a gadolinium gallium garnet substrate. The lattice mismatch between the substrate and the garnet resulted in broken inversion symmetry in the garnet layer. Since this substrate is centrosymmetric, nonmagnetic, and transparent at both the fundamental

and second harmonic wavelengths in their experiment, the SHG signal from this sample is dominated by that of the garnet layer. From this layer, the SHG signal contains both crystallographic (χ_{cr}) and magnetic (χ_{magn}) components that interfere with each other: $I_{2\omega} \propto |\chi_{cr} \pm \chi_{magn}|^2$. The $\pm$ depends on the direction of the magnetization, which changes from domain to domain. Therefore, this interference produces contrasts in the intensity of different domains in the SHG image. Their experiment used a transmission geometry at normal incidence. Due to the Faraday effect, the rotation of the polarization of light caused by a perpendicular magnetic field, only the component of the magnetization perpendicular to the plane of the film can be extracted from linear imaging, while the in-plane magnetization component can be probed using nonlinear imaging. Hence, nonlinear imaging can provide complementary magnetic information to linear imaging.

In Figure 2.1, Kirilyuk et al. show both a linear image and several SHG images taken at different incoming polarizations of light [16]. The two colors in the linear image in Figure 2.1(a), two different intensities of the linear response, represent two different magnetic domains, with magnetization pointed up or down perpendicular to the plane of the film. The SHG images in Figure 2.1(b)-(f), however, reveal four different intensities of second harmonic light, shown as four different colors. These four domains are labeled in Figure 2.1(c). Each domain represents a different in-plane direction of the magnetization. The dashed lines represent the starting positions of domain boundaries, at 0° input polarization in Figure 2.1(b). The remaining SHG images, Figure 2.1(c)-(f), were taken at input polarizations of 10°, 35°, 90°, and 145°, respectively. We can see that the domains shift laterally as the input polarization is rotated. Rotational anisotropy measurements allow for the determination of the in-plane direction of the magnetization in each domain. Combined with the information about the perpendicular direction of the magnetization from the linear image, this group was able to construct the orientations of the magnetization vectors of each of the four domains (see Figure 2.2). Their paper demonstrated the additional information that can be extracted from nonlinear (in this case, MSHG) imaging that cannot be obtained by conventional linear microscopy.

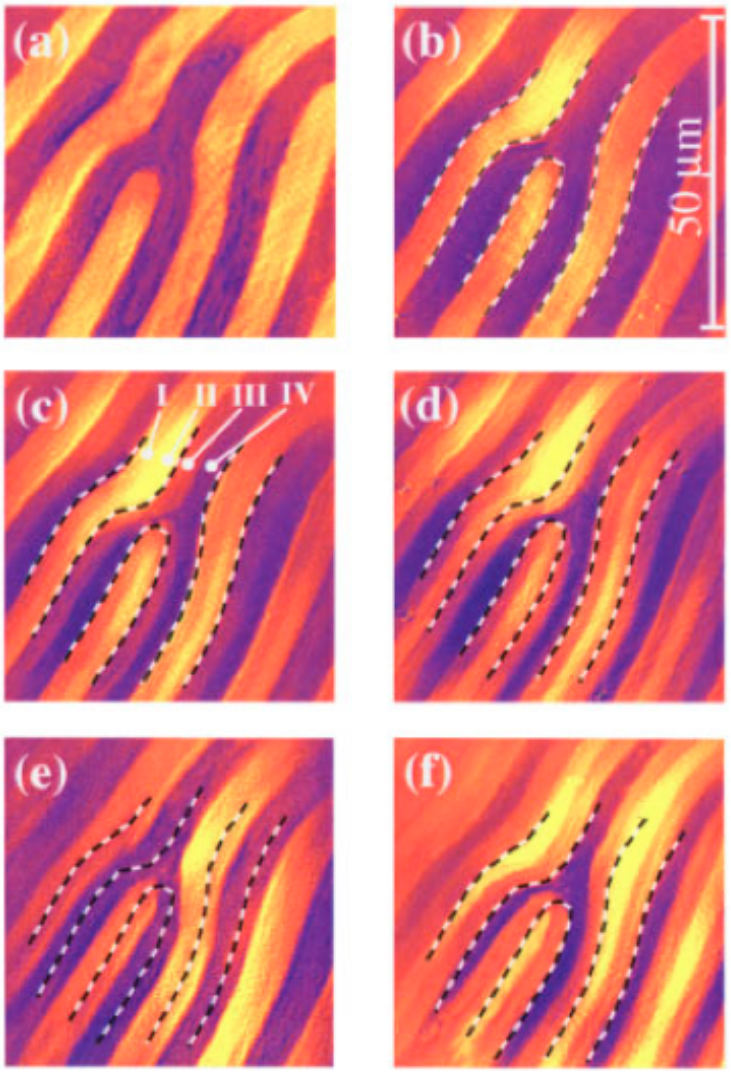

FIGURE 2.1: Images of a garnet film from Kirilyuk et al. Different colors represent different SHG intensities. (a) The linear image shows two different intensities of the linear response, indicating two different magnetic domains oriented up and down with respect to the direction perpendicular to the plane of the garnet film. The SHG images were taken at input polarizations of (b) 0°, (c) 10°, (d) 35°, (e) 90°, and (f) 145°. From the SHG images, we see that there are four different magnetic domains, each with a different in-plane magnetization direction. The domains shift in the lateral direction as the input polarization is varied. (Image taken from [16].)

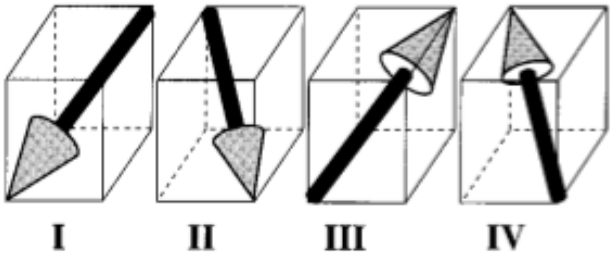

FIGURE 2.2: Orientation of the magnetization vectors of each of the four magnetic domains, as indicated in Figure 2.1(c). (Image taken from [16].)

2.2 Magnetic Force Microscopy of Magnetic Topological Insulators

While no previous studies of MSHG imaging have been done on magnetic TI systems, there have been experiments performed on these materials using magnetic force microscopy (MFM). Wang et al. used MFM imaging to visualize ferromagnetic domains of both single-crystal and thin-film samples of Cr-doped $(Bi_{0.1}Sb_{0.9})_2Te_3$ [17]. Multiple domains form in a ferromagnet to minimize magnetostatic energy. The properties of magnetic domains and domain walls in magnetic TIs are largely unknown. Using cryogenic MFM, Wang et al. observed the formation of bubble-like magnetic domains in both single crystals and thin films. The MFM signal is the change in the frequency of the cantilever as the tip scans across the sample. The MFM images contain bright/dark patches, which represent repulsive/attractive interactions between the MFM tip and the sample, and therefore indicate different magnetic domains. The size of domains in the single crystals were ~ 5 μm and the width of domain walls were ~ 2 μm. In contrast, the thin films had domains of size ~ 500 nm and domain walls of width $\sim 150 - 300$ nm. The spatial resolution of the MFM tip is ~ 100 nm [17].

Example MFM images of a single crystal sample at 5.4 K are shown in Figure 2.3. Bubble-like magnetic domains of size ~ 5 μm can be observed and the width of the domain walls are ~ 2 μm. Figure 2.3(a) is an image taken at zero field, and the cantilever

frequency profile along the orange line is plotted in Figure 2.3(e) as a function of distance along the line. The large domain wall width does not agree with the Bloch wall model and therefore suggests unconventional domain wall structure or a curved domain wall under the surface [17]. In Figure 2.3(b)-(d), a perpendicular magnetic field is applied with increasing magnitude. As the magnetic field strength increases, the magnetic domains with moments in the plane of the sample shrink to zero. The image in Figure 2.3(d) is uniform, indicating that the sample is in a single-domain state with moment perpendicular to the sample (in the direction of the applied field).

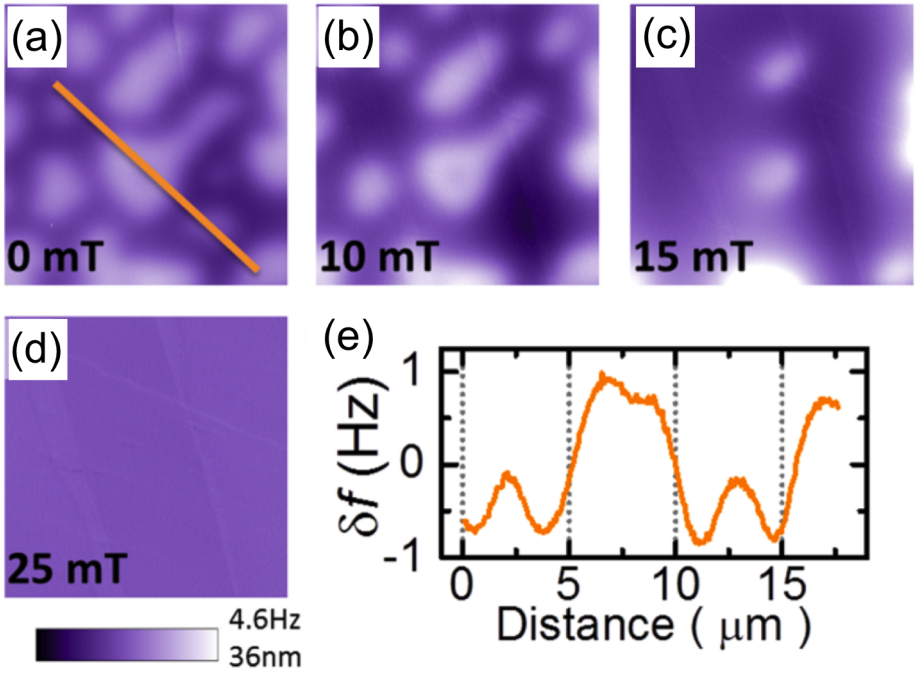

FIGURE 2.3: MFM images of single crystal Cr-doped $(Bi_{0.1}Sb_{0.9})_2Te_3$ taken at 5.4 K. (a) We can see bubble-like magnetic domains of size ~ 5 μm and domain walls of width ~ 2 μm. A magnetic field of strength (b) 10 mT, (c) 15 mT, and (d) 25 mT is applied perpedicular to the sample plane. The size of domains with in-plane moments shrinks to zero and in (d), the sample reaches a single-domain state with perpendicular moment. (e) Cantilever frequency plotted as a function of distance along the orange line in (a). (Figure from [17].)

2.3 Our SHG Imaging Setup

To perform SHG rotational anisotropy and imaging experiments, we used a Ti:sapphire amplified laser system (KM Labs Wyvern) with approximately 50-fs pulses centered at 785 nm at a repetition rate of 30 kHz. It is necessary for us to use a pulsed laser in order to achieve a high enough peak power for SHG experiments. The total power from the laser was attenuated using beam splitters and neutral density filters so that the average power reaching the sample was no higher than 3 mW to prevent sample damage. All experiments were performed in a transmission geometry with the laser beam at normal incidence to the sample. A half-wave plate was placed in front of the sample to control the incoming polarization of the beam, and a polarizer was placed after the sample to set the polarization of transmitted light that was detected. Both the wave plate and polarizer were controlled by a stepper motor so that they could rotate together, which made it possible to perform rotational anisotropy measurements efficiently.

Figure 2.4 is a picture of our SHG imaging setup. A diagram of all of the optical components in our setup is shown in Figure 2.5. A 20 cm focal length lens focused the beam onto the sample, producing a focal spot of ~ 50 μm in diameter. The transmitted light was collected into a 50$\times$ microscope objective. After passing through the objective and the polarizer, the light entered a CCD camera, which produced a digital image. For rotational anisotropy measurements, the CCD camera was replaced with a photomultiplier tube (PMT). The signal from the PMT was connected to a lock-in amplifier that was referenced to the repetition frequency of the laser. When measuring the SHG signal, two 390 nm shortpass filters were placed in front of the CCD or PMT. During alignment and focusing, a white light source was used to illuminate the sample for viewing with the CCD. Both the sample and the objective were mounted on micrometer translation stages to allow for precision alignment of the sample in the x, y, and z directions.

During our experiments with EuS/Bi_2Se_3 heterostructures, the sample was mounted in a cryostat kept under vacuum and cooled with liquid helium. A ring-shaped neodymium

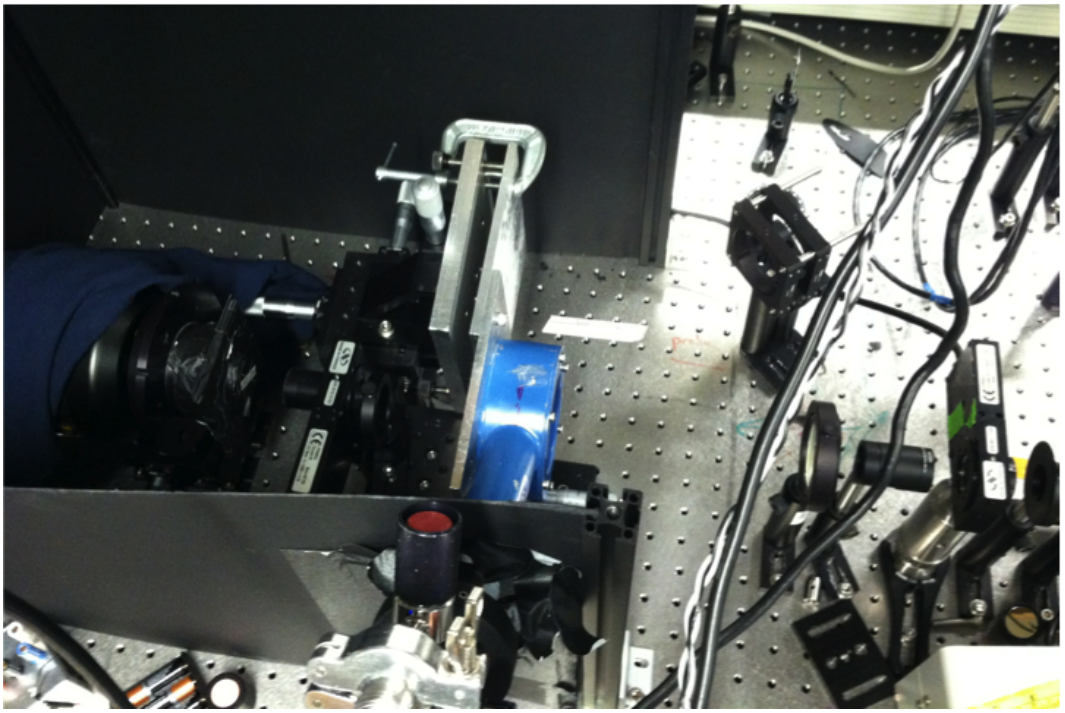

FIGURE 2.4: Picture of our SHG imaging setup.

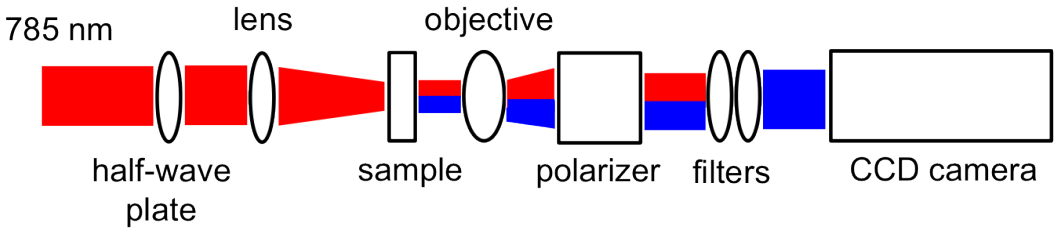

FIGURE 2.5: Diagram of the optical components in our SHG imaging setup. See the text for more detail. During rotational anisotropy measurements, the CCD camera was replaced with a PMT, which was connected to a lock-in amplifier.

magnet was used to produce a magnetic field at the sample. By altering the position of the magnet relative to the sample, we could apply either an in-plane or out-of-plane magnetic field. The experiments with monolayer MoS_2 were performed in ambient conditions without a magnetic field.

2.3.1 Improvements to Our SHG Imaging Setup

I began my thesis work in September 2015 by making improvements to the existing SHG imaging setup in the Gedik lab. When I arrived, one of the issues that had not been

resolved was that ambient light was reaching the CCD camera and obscuring the SHG signal. To solve this problem, I built a light-tight black box to enclose the SHG setup, which is shown in Figure 2.6. The box consisted of black cardboard and posts and was covered with blackout fabric. The only opening was a small hole through which the laser light entered. This improvement eliminated the ambient light reaching the CCD. However, stray light from laser reflections from optics within the box was still present in the CCD images. To fix this, I built a shield out of black cardboard and cut a hole the size of the filter tube that holds the 390 nm SHG filters. I then taped the shield to the aperture of the CCD and taped the filters to the shield using black tape all around the edges so that no light could reach the CCD except by first entering through the filters. When there was even a small gap, laser light was able to get through and obscure the SHG signal. A picture of the shield is shown in Figure 2.7. This final improvement eliminated all extraneous light from the images, so we were then able to proceed with SHG imaging.

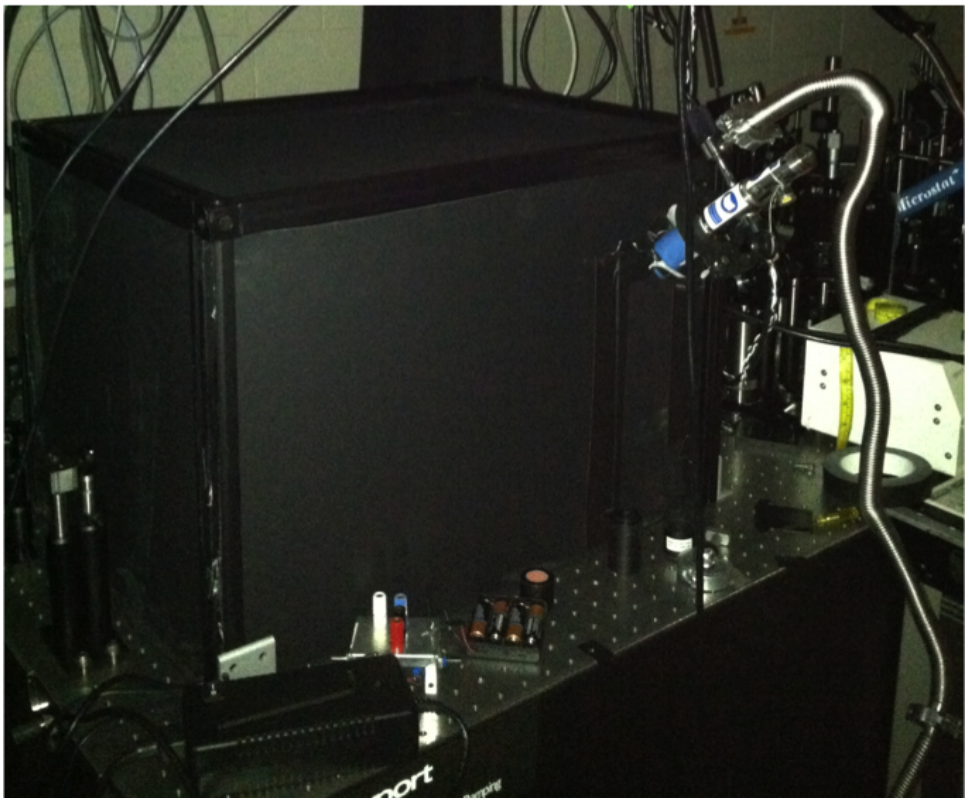

FIGURE 2.6: Picture of the black box enclosing our SHG imaging setup.

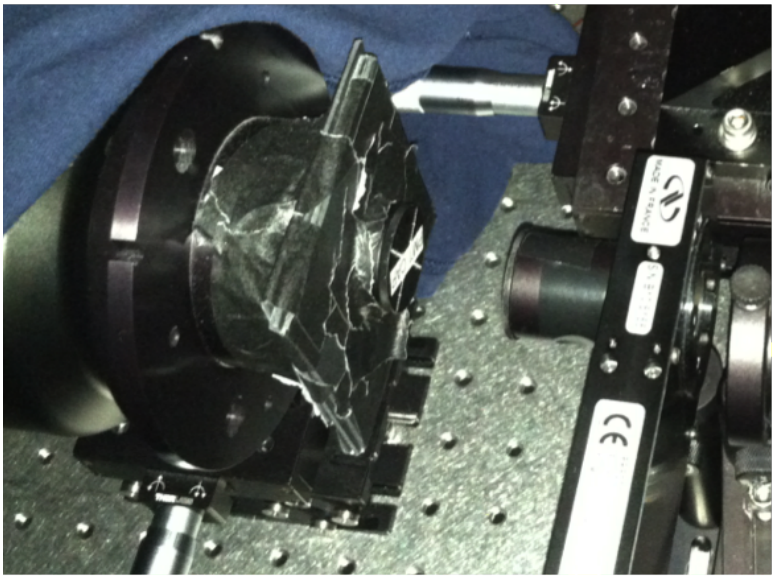

FIGURE 2.7: Picture of the shield taped to the aperture of the CCD camera. The two 390 nm filters were taped to the front of the shield. A cover can be screwed onto the filter to protect the CCD camera from exposure to the room lights.

Another problem with the setup was that the objective, a Mitutoyo model, was altering the polarization of the light that passed through it, which negatively affected the SHG rotational anisotropy measurements. This Mitutoyo objective was not specifically designed for polarization measurements. Since preserving the polarization is key in our experiments, during the fall semester we purchased a new objective from Olympus designed to be distortion free. The new Olympus objective improved the SHG rotational anisotropy data. However, this objective has a smaller numerical aperture (0.50) than that of the old Mitutoyo objective (0.55), and the images produced are not quite as clear. For comparison, in the next chapter I will present SHG images of MoS_2 that were produced using the two different objectives.

2.4 Sample Growth

The two material systems that I worked with in this thesis were MoS_2 and EuS/Bi_2Se_3, discussed in Chapters 3 and 4, respectively. The EuS/Bi_2Se_3 thin films were grown by Ferhat Katmis of Jagadeesh Moodera's group at MIT using molecular beam epitaxy

(MBE). The MBE growth was performed in an ultrahigh vacuum environment (10^{-10} torr) for high purity growth [6]. In MBE, beams of atoms in the gaseous phase are deposited on the substrate where they become part of a growing solid layer. The growth rate is extremely slow so MBE can produce samples that are only a few atomic layers thick to great precision. Each beam of different elements can be turned off and on quickly with a shutter, so MBE allows for high precision over the sample thickness and composition. The monolayer MoS_2 sample was grown by Yi-Hsien Lee, a former member of Jing Kong's group at MIT, using the method of chemical vapor deposition (CVD). In CVD growth, the desired material is vaporized in a vacuum chamber and is deposited on the surface of the substrate.

All samples were grown on sapphire substrates so that they could be used in transmission experiments, since sapphire is transparent. Moreover, sapphire has a high thermal conductivity so it allows samples to be cooled effectively when the sample is mounted in the cryostat and cooled with liquid helium. The MoS_2 sample was a single monolayer in thickness. The EuS/Bi_2Se_3 sample consisted of 7 nm of EuS and 7 QL of Bi_2Se_3.

Chapter 3

SHG Imaging of MoS_2

As one way of verifying the functionality of our SHG imaging setup, we performed SHG imaging on monolayer MoS_2 and compared the results to the SHG images by Yin et al. (see Figure 1.8). In this chapter, we present our SHG imaging data of MoS_2 using first the Mitutoyo objective and then the Olympus objective.

3.1 Calibration

To determine the scaling in our images, we first had to perform calibration tests. Focusing on a particular feature on the sample, we incrementally moved the sample using the micrometer stages and recorded the pixel coordinates of the feature in the image. The slope of this set of data points gave us the corresponding number of microns per pixel in our images. Figure 3.1 shows one such calibration plot. We found a value of ~ 0.5 μm/pixel.

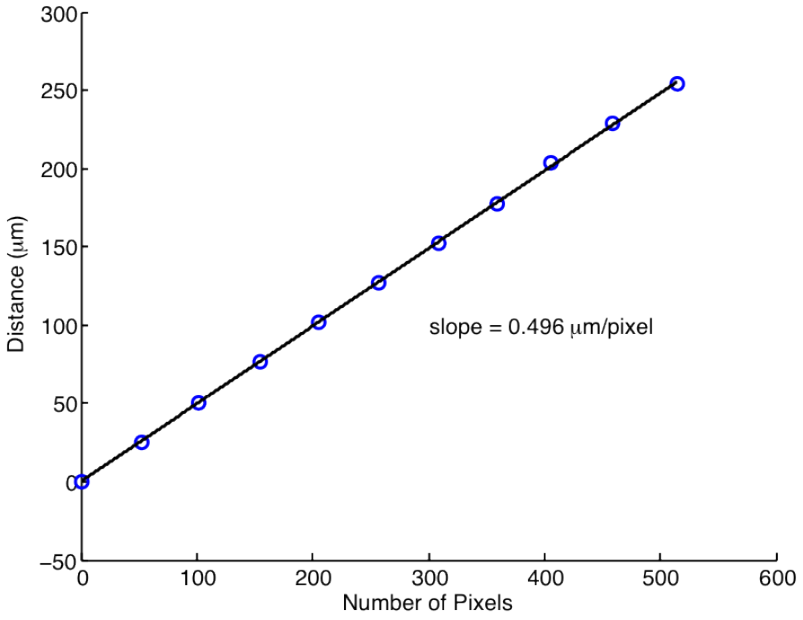

FIGURE 3.1: Calibration plot. The slope corresponds to the number of microns per pixel in our images, which is ~ 0.5 μm/pixel.

3.2 SHG Imaging of MoS_2 Using the Mitutoyo Objective

A set of SHG images taken at room temperature using our old Mitutoyo objective is shown in Figure 3.2. These images are all in the parallel polarized geometry, meaning that the polarization of light that we collect in the CCD camera is the same direction as the polarization of light that is incident on the sample. All images were collected using a 30 s exposure time. Each successive image has an input polarization that is rotated by 10°. Due to the symmetry of the MoS_2 crystal structure, we show only 60° of rotation. Similar to the published data from Yin et al., we see clear single crystal grains separated by grain boundaries. We can observe variation in the sizes of individual grains, ranging from about 5 μm to 20 μm in diameter. Tracking a single grain (circled in white in Figure 3.2), we see that its intensity varies as we rotate the polarization, as expected. (This effect of the variation in SHG intensity with polarization angle is more clearly seen in rotational anisotropy measurements, such as in Figure 1.6.) The SHG signal of this

single grain reaches its maximum intensity around 0° (and 60°) input polarization and its minimum around 30° (30° away), which agrees with the rotational symmetry of MoS_2 crystals. (Each petal of a rotational anisotropy plot is 60° so there is 30° between each successive maximum and minimum.) Therefore, this set of SHG images suggests that the single grains we observe are each single crystals. By using the polarization direction of the maximum and minimum SHG intensities of a single grain, we can determine the exact orientation of that grain, i.e. the direction of the crystal axes. The occassional extra bright spots in the images are likely due to impurities.

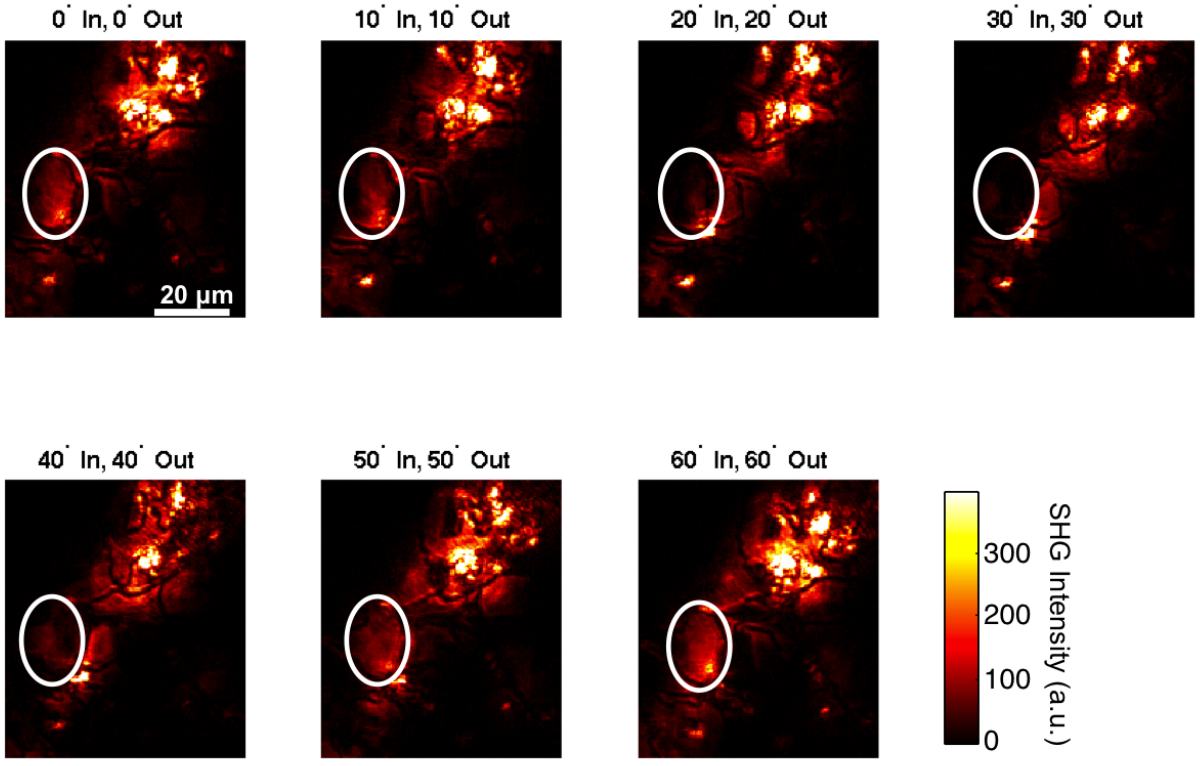

FIGURE 3.2: Room temperature SHG images of MoS_2 in the parallel polarized geometry taken with the Mitutoyo objective. Each image was collected with a 30 s exposure time and the polarization of light was rotated by 10° from one image to the next. In the images we can observe distinct crystal grains separated by dark grain boundaries. One of these grains is circled in white. The SHG intensity of the grain varies with polarization angle, as would be expected from rotational anisotropy measurements. Different grains reach their maximum SHG intensities at different polarization angles, indicating that the grains are oriented in different directions.

Figure 3.3 shows the same location on the MoS_2 sample but the SHG images were

taken in the cross polarized geometry, meaning that the detected polarization was perpendicular to the input polarization at each angle. Similar to the parallel polarized data, the cross polarized images also reveal the symmetry of the MoS_2 crystal grains. The same grain is highlighted in these images as well. Note that the SHG intensity of this grain is now brightest around 30° and weakest around 0° (and 60°), the opposite pattern of the parallel polarized images, which would also be expected from rotational anisotropy measurements.

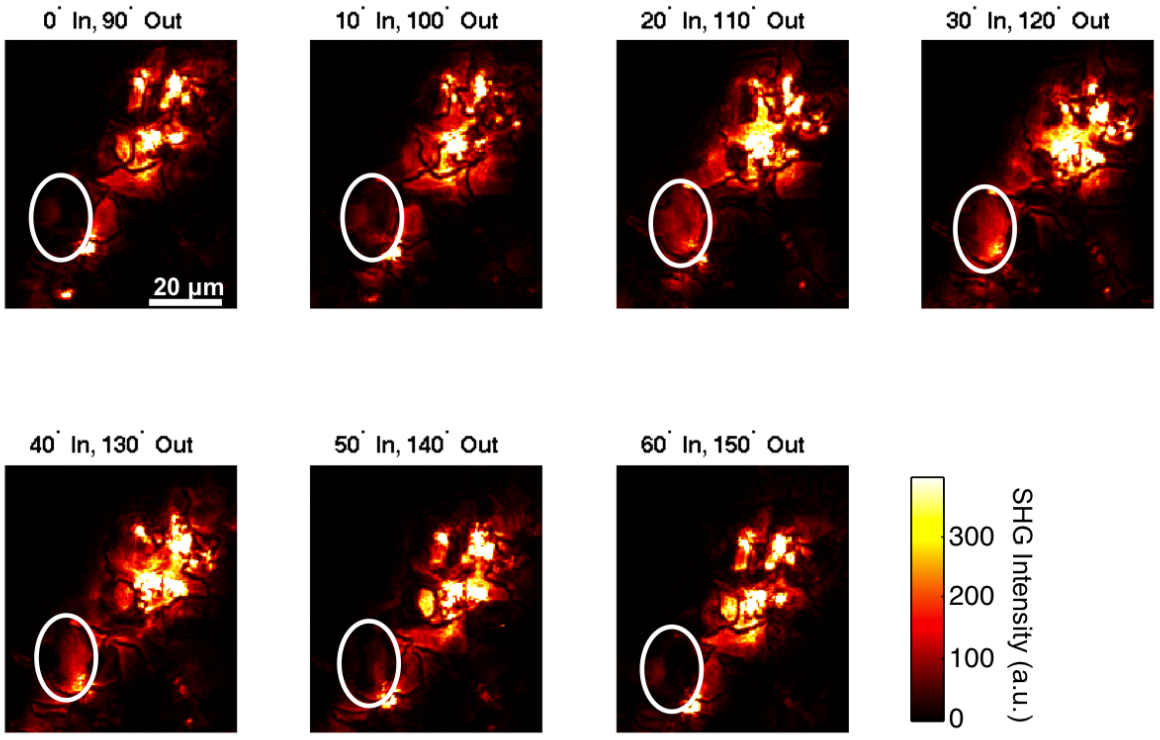

FIGURE 3.3: Room temperature SHG images of MoS_2 in the cross polarized geometry taken with the Mitutoyo objective. The experimental parameters are the same as those for the parallel polarized data above. The same crystal grain is circled in white for comparison.

To visualize the variation in the sample surface, we scanned across the sample and recorded images every 12.5 μm. The input and output polarization directions remained fixed throughout the scan. The SHG images from the position scan are shown in Figure 3.4. We can see that the individual grains vary in both size and shape across the sample.

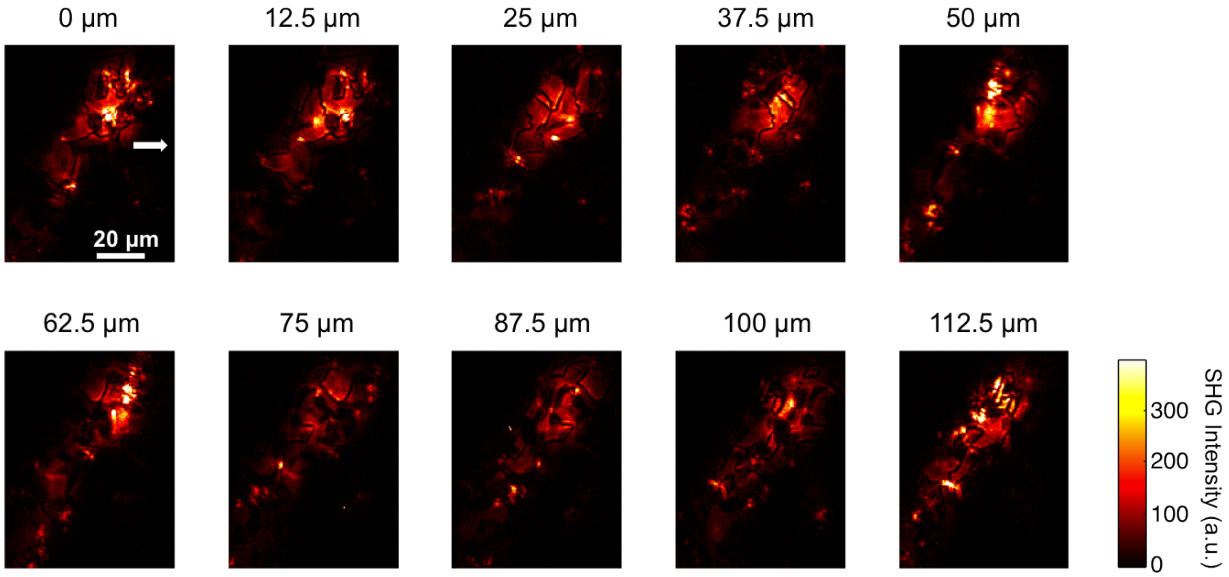

FIGURE 3.4: SHG images of MoS_2 taken with the Mitutoyo objective. The input and output polarizations were kept fixed as the sample position was translated with respect to the focal spot. Each successive image was translated by 12.5 μm to the right. The numbers above the images indicate the distance from the initial sample position. We can observe a variety of sizes and shapes of crystal grains across the MoS_2 sample.

Figure 3.5(a) shows one image from this position scan and examines the grain boundaries more closely. Figure 3.5(b) shows a cross section of a single grain boundary (the location of the boundary on the sample is indicated by the white line in Figure 3.5(a)). From the cross section, we can see that the width of the boundary is about 2 pixels, which is about 1 μm (since 1 pixel corresponds to approximately 0.5 μm in our images as determined by the calibration data above). This is at the limit of our resolution so we cannot make any detailed conclusions about nature of the boundary based on its profile in Figure 3.5(b). However, our images can at least give the approximate width of the boundary. It is important to note that our imaging resolution is ultimately limited by diffraction, that is, the wavelength of SHG light, 400 nm.

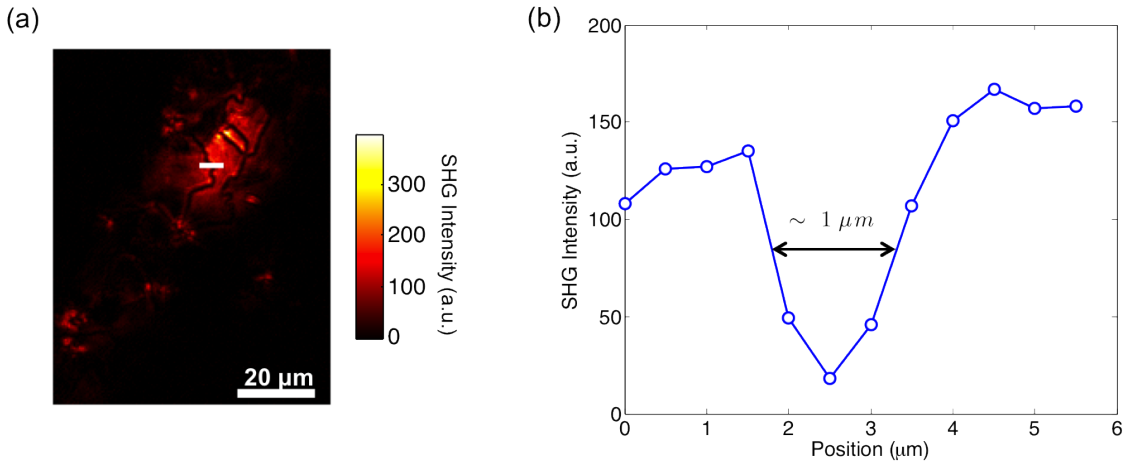

FIGURE 3.5: (a) A single image from the position scan in Figure 3.4. (b) Cross section of a grain boundary. The SHG intensity is plotted as a function of distance along the white line in (a). The grain boundary (indicated by the dip in intensity) has a width of ~ 1 μm.

3.3 SHG Imaging of MoS_2 Using the Olympus Objective

In contrast with the previous images, we now show SHG images produced using the new Olympus objective. A representative set of parallel polarized images is shown in Figure 3.6. The quality of the images is not as high as the images taken with the old Mitutoyo objective, even after careful focusing and alignment, due to the smaller numerical aperture of the Olympus objective compared to the Mitutoyo objective. However, the Olympus objective is better at preserving the polarization of the signal, which we have verified by rotational anisotropy measurements. In the parallel polarized set of SHG images in Figure 3.6, tracking the highlighted grain in the center of the image, we see that the intensity of that grain clearly varies as we rotate the polarization. It reaches its maximum intensity around 0° (and 60°) and its minimum around 30°, again confirming the symmetry of the MoS_2 crystal structure. Though the image quality is not as high, the Olympus objective is more accurate in terms of measuring polarization. Since polarization is one of the most important quantities in our SHG measurements, we will continue to use this new Olympus objective. All of the images in the following chapters were taken

using the Olympus objective.

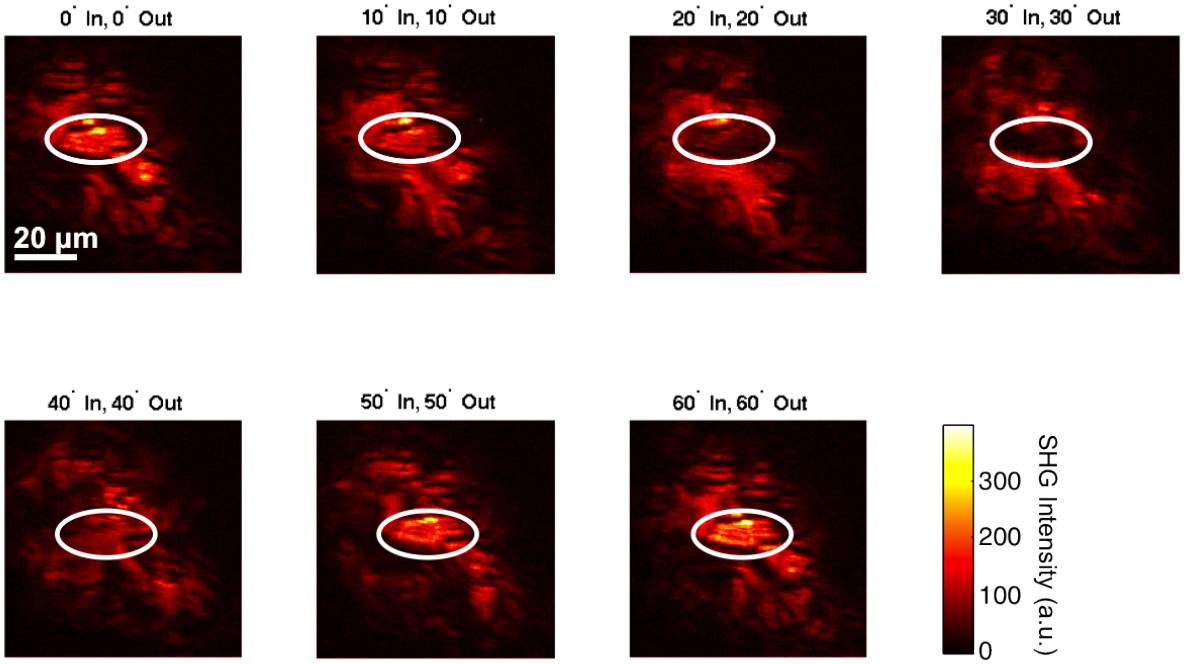

FIGURE 3.6: SHG images of MoS_2 in the parallel polarized geometry taken with the Olympus objective. These images are not as clear as those taken with the Mitutoyo objective because the Olympus objective has a smaller numerical aperture than the Mitutoyo objective. However, the Olympus objective better preserves the polarization of the signal. Looking at a single grain (circled in white), we can clearly observe the variation in the SHG intensity with polarization angle.

Our MoS_2 SHG imaging data confirms that our SHG images are similar to those in the published data [13] and reveals the polycrystalline structure of our MoS_2 sample. Moreover, we can use SHG imaging to map out the exact orientation of the different crystal grains. SHG imaging is therefore a useful tool for visualizing crystal grains and grain boundaries and for spatially mapping out the orientations of crystal grains in two-dimensional non-centrosymmetric materials. This MoS_2 data confirms that we have a fully functional SHG imaging setup and that we can now proceed with our original goal of using SHG imaging to study the magnetic TI system EuS/Bi_2Se_3.

Chapter 4

SHG Imaging of EuS/Bi_2Se_3

The goal of this experiment was to use MSHG imaging to visualize magnetic domains in EuS/Bi_2Se_3 heterostructures and possibly chiral edge states at the domain boundaries as well. Chiral edge states in magnetic topological insulators have yet to be experimentally observed. We have not been able to see domains in EuS/Bi_2Se_3 so far. This chapter describes the progress we have made towards this goal, discusses reasons for why we have not seen domains, and presents our next steps for this experiment. All of the images shown in this chapter were taken with the new Olympus objective.

4.1 Room Temperature SHG Imaging of EuS/Bi_2Se_3

First, we present SHG images taken at room temperature. Since the Curie temperature of EuS is 17 K, at room temperature there is no magnetism in the sample. As discussed in Chapter 1, both EuS and Bi_2Se_3 are centrosymmetric materials so the bulk of each of these materials will not contribute significantly to the SHG signal, and therefore the main SHG contribution will be from the interface between the two layers where inversion symmetry is broken. Since EuS does not produce an SHG signal (as verified by SHG RA measurements of a EuS film without the Bi_2Se_3 layer), SHG measurements of EuS/Bi_2Se_3

films at room temperature will therefore reveal the crystalline symmetry of Bi_2Se_3 at the interface.

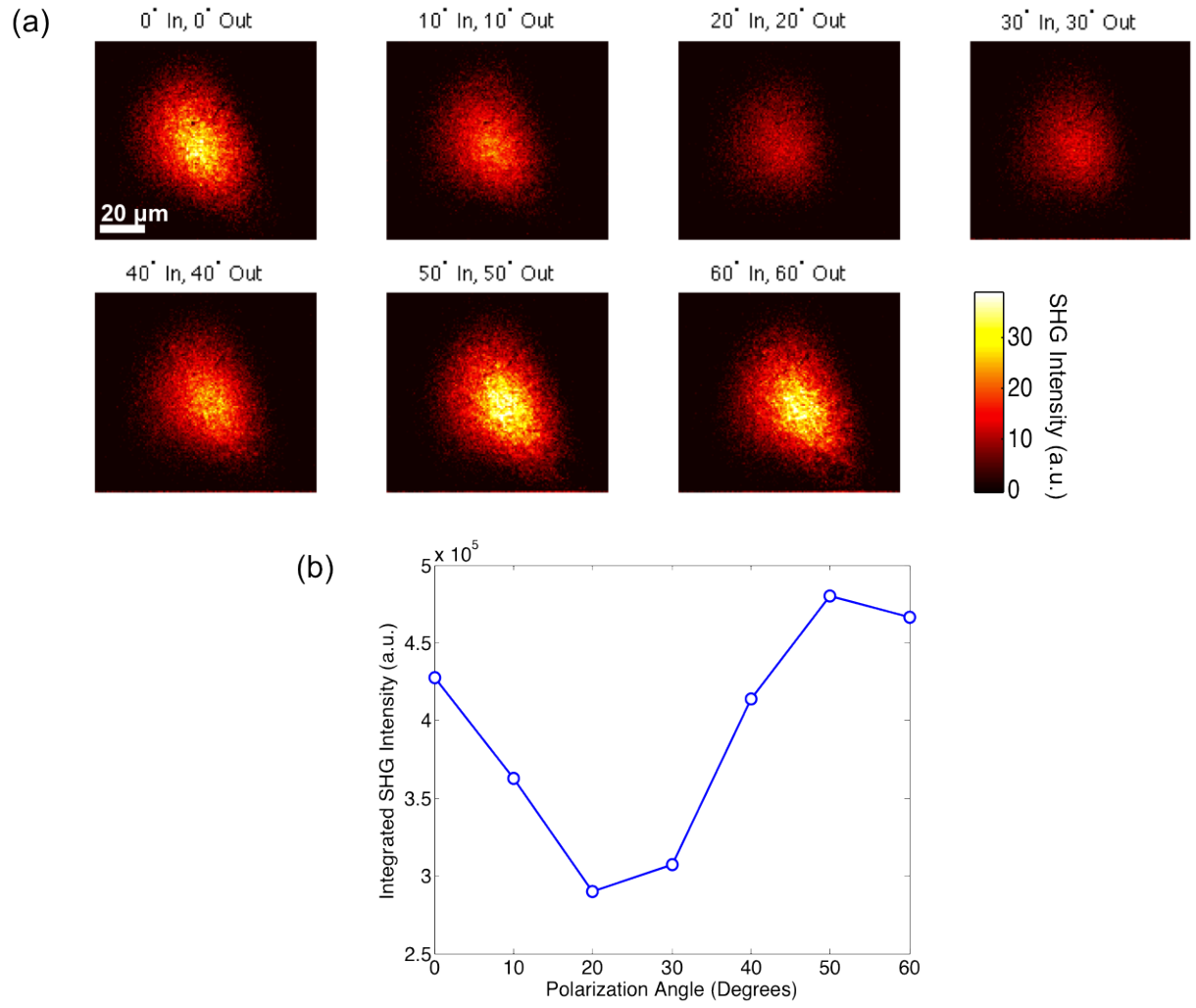

FIGURE 4.1: (a) SHG images of EuS/Bi_2Se_3 in the parallel polarized geometry at room temperature. Each image is uniform so our EuS/Bi_2Se_3 sample is either a single crystal grain or all of the grains are aligned in the same direction. (b) The sum of the counts from each image in (a) plotted as a single point versus polarization angle. The trend in SHG intensity from the SHG imaging data agrees well with rotational anisotropy measurements (Figure 1.6).

Shown in Figure 4.1(a) is a set of SHG images in the parallel polarized geometry. The images are uniform, which suggests that the sample is a single crystal grain, or all crystal grains are aligned in the same direction. The varying intensity of the SHG signal with a period of 60° agrees with the rotational symmetry of Bi_2Se_3 shown in Figure 1.6. The SHG signal appears brightest around 50° and weakest around 20°. Figure 4.1(b) shows

the sum of the counts from the CCD camera in the field of view shown in Figure 4.1(a). This is effectively recreating the rotational anisotropy measurements made with the PMT, which takes in all of the SHG signal coming from the sample (since it is not spatially sensitive) and records a single intensity value for each input polarization angle. The data shown in Figure 4.1(b) corresponds to one petal of the RA pattern. The maximum at 50° indicates that the mirror plane of the Bi_2Se_3 crystal is in that direction. We can see that the variation in the SHG signal summed from the CCD counts agrees well with the symmetry of the RA pattern in Figure 1.6 of the surface crystal structure of Bi_2Se_3.

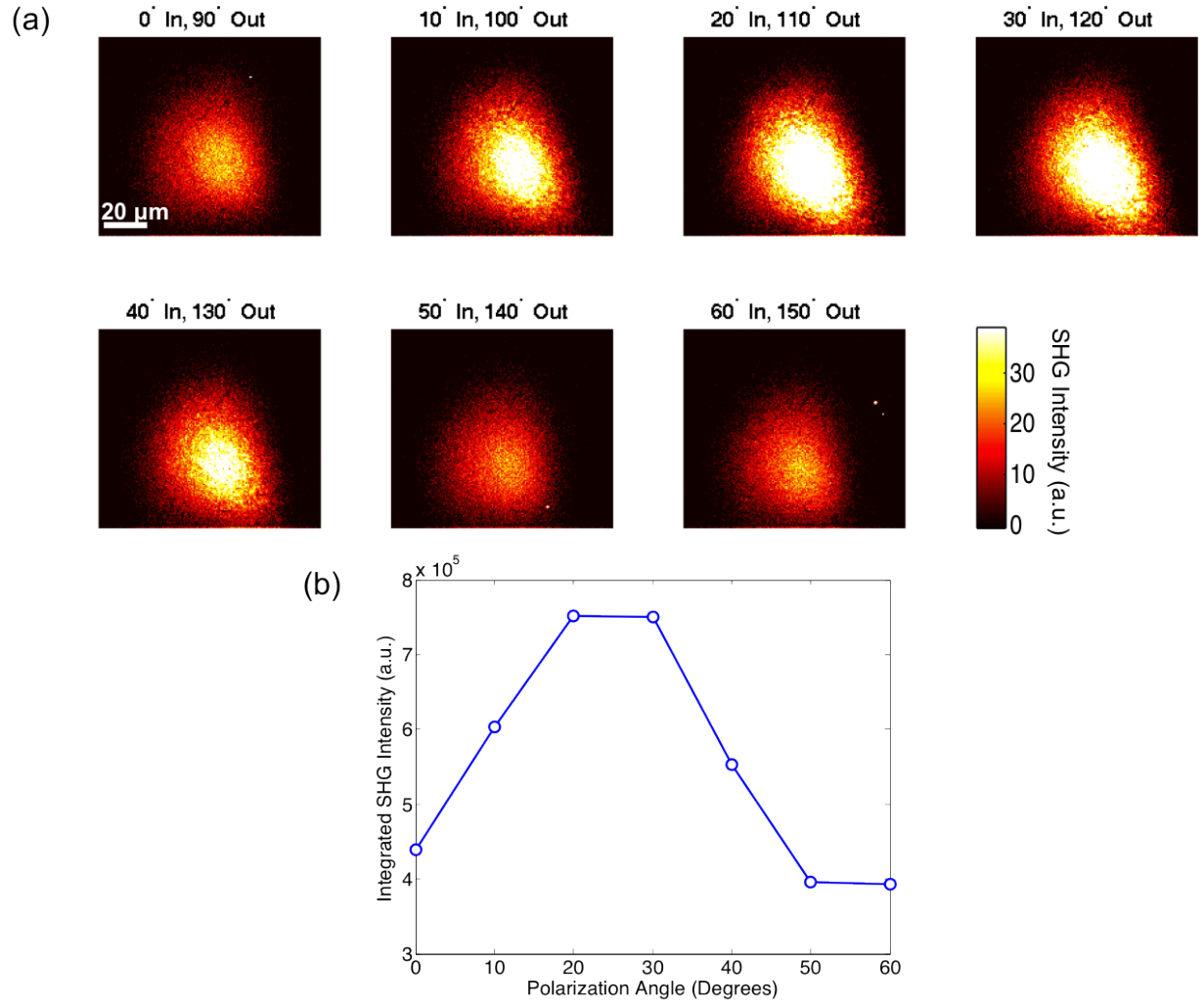

FIGURE 4.2: (a) SHG images of EuS/Bi_2Se_3 in the cross polarized geometry at room temperature. (b) The sum of the counts from each image in (a) plotted as a single point versus polarization angle. The cross polarized data follows the opposite trend of the parallel polarized data, which is expected from rotational anisotropy measurements.

Figure 4.2 shows SHG images taken in the cross polarized geometry. The plot in Figure 4.2(b) shows the sum of the counts from the CCD at each input polarization angle and also agrees with the RA data of Bi_2Se_3. Notice that the maximum in the SHG intensity occurs around 20° and the minimum around 50°, the opposite trend of the parallel polarized plot in Figure 4.1(b). This is again a consequence of the variation in SHG intensity of the Bi_2Se_3 crystal structure as a function of the input polarization angle of light and can be verified by rotational anisotropy measurements.

4.2 SHG Imaging of EuS/Bi_2Se_3 at 4 K

Next, we cooled the EuS/Bi_2Se_3 sample to 4 K (below the Curie temperature of EuS) and repeated the SHG imaging measurements. Now there should be contributions to the SHG signal from both the crystal structure and magnetic structure at the interface, so we expect that we may see the formation of magnetic domains in our SHG images. However, the images still appear uniform and we have yet to observe any signs of magnetic domains.

To try to improve our resolution, we varied the focus of the images, which is shown in Figure 4.3. We adjusted the distance of the sample with respect to the objective. The total distance moved with respect to the position of the sample in the first image is labeled in microns above each image. We still do not see any evidence of magnetic domains, which would appear as regions of contrasting intensity in the SHG images.

4.3 SHG Imaging of EuS/Bi_2Se_3 at 4 K in a Magnetic Field

We also performed SHG imaging measurements in a magnetic field and compared the data to the rotational anisotropy data of EuS/Bi_2Se_3 by Lee et al. (Figure 1.10). Figure 4.4 shows the summed counts of SHG images (similar to Figure 4.1(a) and Figure 4.2(a))

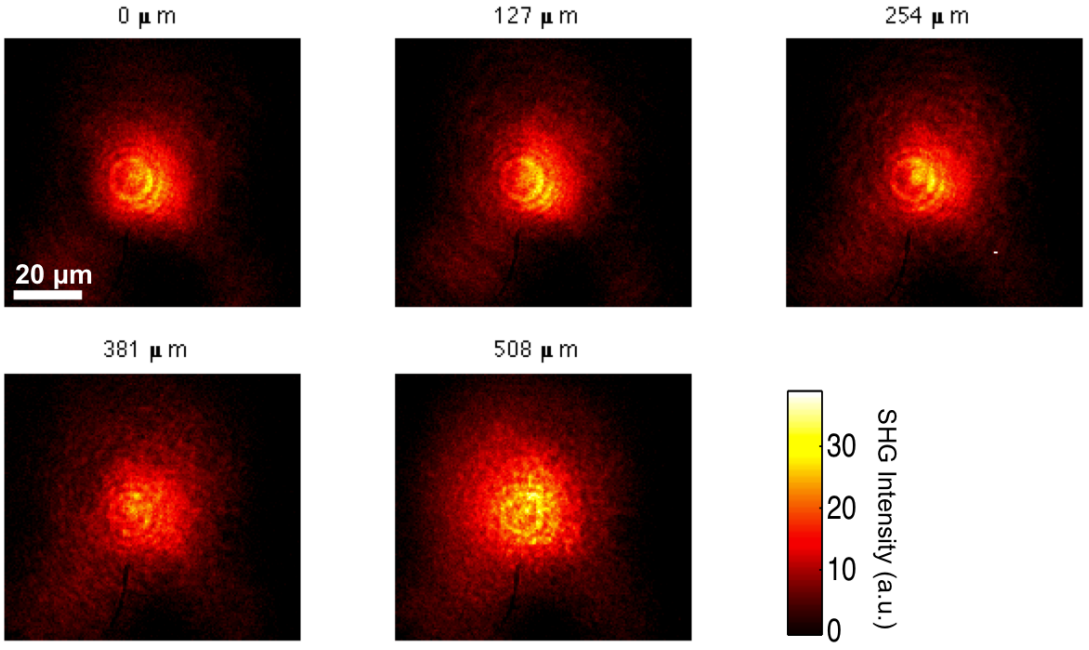

FIGURE 4.3: SHG images of EuS/Bi_2Se_3 at 4 K. The value in microns above each image represents the distance moved with respect to the position of the sample in the first image. Despite trying to improve the resolution by varying the focus, we do not see any evidence of the formation of magnetic domains.

taken in an in-plane magnetic field. The blue curve represents an applied field of +300 Gauss and the red curve represents an applied field of −300 Gauss. Both data curves follow a similar variation in SHG intensity with a period of 60°, which is consistent with the crystal symmetry of the Bi_2Se_3 at the interface. We also see the effect of the additional magnetic component to the SHG signal, as the blue and red curves do not overlap. The trend of alternating blue and red for which data has a lower intensity at the minimums agrees with the previous RA data in Figure 1.10. However, the red data points are always at a higher intensity at the maximums, which is not as expected. Additionally, there is an overall increase in the SHG signal with larger polarization angle.

One possible reason for the inconsistencies in the data in Figure 4.4 is long-term fluctuations of our laser. Since each image takes time to collect plus time to rotate the polarization, our measurements are subject to any change in the laser power or position of the beam over time. An increase/decrease in laser power would correspond to an

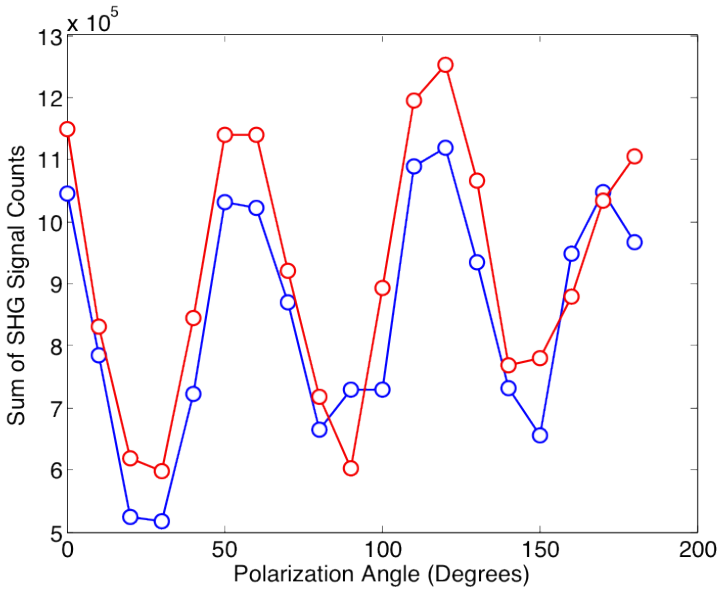

FIGURE 4.4: SHG images of EuS/Bi_2Se_3 taken at 4 K in an in-plane magnetic field. The blue curve has an applied field of +300 Gauss and the red curve has a field of −300 Gauss. The data approximately agrees with rotational anisotropy data of this material in Figure 1.10. However, there are some inconsistencies in this data that might be due to long-term laser fluctuations.

increase/decrease in the intensity of SHG produced. More precisely, since SHG is a nonlinear process, a factor of 2 increase in laser power corresponds to a factor of $2^2 = 4$ increase in SHG signal. Therefore, any fluctuations in the laser power become amplified in the SHG signal. A slight shift in the beam location would slightly alter how the beam travels through the optics (for example, the beam may no longer travel directly throught the center of a lens), which could affect how much power is delivered to the sample as well as how much SHG signal is ultimately collected into the CCD camera. We may be able to correct for artifacts in the data due to laser fluctuations by monitoring the laser power during experiments.

4.4 Discussion and Future Work

The above SHG imaging data taken in a magnetic field demonstrates that we are sensitive to the magnetism induced at the interface between the EuS and Bi_2Se_3 layers. However,

we have not yet seen any evidence of the formation of magnetic domains in our SHG images. One possibility for why we have not seen domains is that the SHG signal is too weak compared to the background signal. It is important to note that the SHG signal in this material system is much weaker than the SHG signal from non-centrosymmetric MoS_2. To test this, we can take images with much longer exposure times and see if any additional features are revealed in the images. We can also increase the laser power that is incident on the sample. However, we must be careful not to exceed the damage threshold of this material, which we determined to be about 5 mW.

A second reason might be that the domains are too small for our resolution. A domain size less than a micron would not be discernable in our images. The study by Wang et al. on a different magnetic topological insulator system found that the average domain size in thin film samples was on the order of 500 nm while the average domain size in single crystals was about 5 μm [17]. However, they used a different material, so it is unknown whether a similar domain size should be expected in EuS/Bi_2Se_3 thin films. Since there have been very few magnetic domain studies done in magnetic topological insulator systems, a typical magnetic domain size remains an open question.

Future work on this experiment may include obtaining single crystal samples of magnetic doped Bi_2Se_3 and performing SHG imaging on them to see if the magnetic domain sizes are large enough for our resolution. To do this, we would need to build a slightly different setup in a reflection geometry rather than a transmission geometry, as described in [9]. The penetration depth of light in single crystal Bi_2Se_3 is $\sim$ 25 nm for 800 nm light and $\sim$ 10 nm for 400 nm light [18]. Therefore, single crystal samples would be too thick for the light travel all the way through the sample to obtain an SHG signal from transmission experiments. Before changing our setup to reflection, we can image other samples of EuS/Bi_2Se_3 thin films with different thicknesses and try to optimize our resolution in the hope of visualizing the magnetic domains at the interface.

Chapter 5

Conclusion

In summary, second harmonic generation imaging can be a useful probe of lattice and magnetic structure at surfaces and interfaces of inversion symmetric materials. SHG can reveal additional information beyond what can be learned from conventional linear microscopy. This technique is promising for the study of quantum materials such as topological insulators and 2D materials. The goal of this thesis was to use SHG imaging to investigate the formation of magnetic domains at the interface of the magnetic topological insulator system EuS/Bi_2Se_3. Lee et al. previously performed SHG rotational anisotropy measurements on this system and found evidence of magnetism induced at the interface. SHG imaging can provide spatial information about the interface magnetism

First, we made significant improvements to the existing SHG imaging setup in the Gedik lab to bring it to full functionality. This included making a black box to enclose the whole setup and a shield for the CCD camera. These improvements succeeded in blocking ambient light and unwanted laser reflections from reaching the CCD camera. We also replaced our Mitutoyo objective with a new Olympus objective that was specifically designed to preserve the polarization of light, which greatly improved our SHG rotational anisotropy data.

As a test of our imaging setup, we performed SHG imaging experiments on monolayer MoS_2, a non-centrosymmetric 2D TMD compound, for which there is SHG imaging data in the literature. Our SHG images agreed well with the previously published results, showing that our MoS_2 sample is polycrystalline. The data also confirmed that SHG imaging is a useful tool for visualizing crystal grains and grain boundaries in 2D non-centrosymmetric materials. Additionally, we can use SHG imaging to map out the exact orientation of each individual crystal grain.

Finally, we performed SHG imaging experiments on EuS/Bi_2Se_3 thin films. At room temperature, which is above the Curie temperature of EuS (17 K), the SHG signal only contains information about the crystal symmetry of Bi_2Se_3 at the interface. The SHG images appeared uniform, indicating that our sample is either a single crystal grain or all of the grains are aligned in the same direction. When we cooled to 4 K, we searched for evidence of the formation of magnetic domains at the interface. Though we can detect magnetism at the interface by SHG rotational anisotropy measurements, we have not been able to visualize magnetic domains in SHG images. Possible reasons for why we have not seen domains include that the SHG signal from this material is very weak and the size of the domains could be smaller than our resolution. A previous study on a different magnetic topological insulator showed that magnetic domains in thin film samples were of size ~ 500 nm, while the domains in single crystals were ~ 5 μm. A future avenue for this project could be to obtain single crystals of our material and change the geometry of our setup to reflection in order to perform SHG imaging experiments on single crystals.

Though we have not been able to visualize the formation of magnetic domains in EuS/Bi_2Se_3 thin films, this thesis project has helped improve and optimize our SHG imaging setup. Our work on the SHG imaging setup paves the way for investigating other interesting quantum materials using SHG imaging.

Bibliography

[1] B. Andrei Bernevig with Taylor L. Hughes. *Topological Insulators and Topological Superconductors*. Princeton University Press, 2013.

[2] Joel E. Moore. The birth of topological insulators. *Nature*, 464(7286):194–198, 03 2010.

[3] Thomas Schäpers. Topological insulators. URL `http://www.vi-ti.de/vi-ti/EN/Research/01-Introduction/01-Introduction_node.html`.

[4] M. Z. Hasan and C. L. Kane. *Colloquium* : Topological insulators. *Reviews of Modern Physics*, 82:3045–3067, Nov 2010.

[5] Y. L. Chen, J.-H. Chu, J. G. Analytis, Z. K. Liu, K. Igarashi, H.-H. Kuo, X. L. Qi, S. K. Mo, R. G. Moore, D. H. Lu, M. Hashimoto, T. Sasagawa, S. C. Zhang, I. R. Fisher, Z. Hussain, and Z. X. Shen. Massive dirac fermion on the surface of a magnetically doped topological insulator. *Science*, 329(5992):659–662, 2010.

[6] Peng Wei, Ferhat Katmis, Badih A. Assaf, Hadar Steinberg, Pablo Jarillo-Herrero, Donald Heiman, and Jagadeesh S. Moodera. Exchange-coupling-induced symmetry breaking in topological insulators. *Physical Review Letters*, 110:186807, Apr 2013.

[7] Qi I. Yang, Merav Dolev, Li Zhang, Jinfeng Zhao, Alexander D. Fried, Elizabeth Schemm, Min Liu, Alexander Palevski, Ann F. Marshall, Subhash H. Risbud, and Aharon Kapitulnik. Emerging weak localization effects on a topological insulator-insulating ferromagnet (Bi_2Se_3-EuS) interface. *Physical Review B*, 88:081407, Aug 2013.

[8] Robert W. Boyd. *Nonlinear Optics*. Academic Press, third edition, 2008.

[9] Darius H. Torchinsky, Hao Chu, Tongfei Qi, Gang Cao, and David Hsieh. A low temperature nonlinear optical rotational anisotropy spectrometer for the determination of crystallographic and electronic symmetries. *Review of Scientific Instruments*, 85(8), 2014.

[10] P. A. Franken, A. E. Hill, C. W. Peters, and G. Weinreich. Generation of optical harmonics. *Physical Review Letters*, 7:118–119, Aug 1961.

[11] Haijun Zhang, Chao-Xing Liu, Xiao-Liang Qi, Xi Dai, Zhong Fang, and Shou-Cheng Zhang. Topological insulators in Bi_2Se_3, Bi_2Te_3 and Sb_2Te_3 with a single dirac cone on the surface. *Nature Physics*, 5(6):438–442, 06 2009.

[12] D. Hsieh, J. W. McIver, D. H. Torchinsky, D. R. Gardner, Y. S. Lee, and N. Gedik. Nonlinear optical probe of tunable surface electrons on a topological insulator. *Physical Review Letters*, 106:057401, Feb 2011.

[13] Xiaobo Yin, Ziliang Ye, Daniel A. Chenet, Yu Ye, Kevin O'Brien, James C. Hone, and Xiang Zhang. Edge nonlinear optics on a MoS_2 atomic monolayer. *Science*, 344 (6183):488–490, 2014.

[14] Ting Cao, Gang Wang, Wenpeng Han, Huiqi Ye, Chuanrui Zhu, Junren Shi, Qian Niu, Pingheng Tan, Enge Wang, Baoli Liu, and Ji Feng. Valley-selective circular dichroism of monolayer molybdenum disulphide. *Nature Communications*, 3:887, 06 2012.

[15] Changmin Lee, Ferhat Katmis, Pablo Jarillo-Herrero, Jagadeesh S. Moodera, and Nuh Gedik. Direct measurement of ferromagnetism induced at the interface of a magnetic topological insulator. Accepted for publication in *Nature Communications*, 2016.

[16] V. Kirilyuk, A. Kirilyuk, and Th. Rasing. A combined nonlinear and linear magneto-optical microscopy. *Applied Physics Letters*, 70(17):2306–2308, 1997.

[17] Wenbo Wang, Fang Yang, Chunlei Gao, Jinfeng Jia, G. D. Gu, and Weida Wu. Visualizing ferromagnetic domains in magnetic topological insulators. *APL Materials*, 3(8):083301, 2015.

[18] J. W. McIver, D. Hsieh, S. G. Drapcho, D. H. Torchinsky, D. R. Gardner, Y. S. Lee, and N. Gedik. Theoretical and experimental study of second harmonic generation from the surface of the topological insulator Bi_2Se_3. *Physical Review B*, 86:035327, Jul 2012.